AGU100 ADVANCING EARTH AND SPACE SCIENCE

Tectonics

RESEARCH ARTICLE
10.1029/2018TC004956

Key Points:
- High-resolution *P* and *S* velocity models reveal a sharp Cordillera-Craton boundary and well-correlated mantle anomalies and crustal domains
- Correlation analysis of mantle velocity with heat flow and gravity data suggests melt depletion and enrichment in lithosphere of western Laurentia
- Kimberlites/lamproites preferentially occurred near the high-velocity gradients marking potential weak zones in continental lithosphere

Supporting Information:
- Supporting Information S1

Correspondence to:
Y. Chen,
yunfeng1@ualberta.ca

Citation:
Chen, Y., Gu, Y. J., & Hung, S.-H. (2018). A new appraisal of lithospheric structures of the Cordillera-Craton boundary region in western Canada. *Tectonics*, *37*. https://doi.org/10.1029/2018TC004956

Received 1 JAN 2018
Accepted 15 AUG 2018
Accepted article online 27 AUG 2018

A New Appraisal of Lithospheric Structures of the Cordillera-Craton Boundary Region in Western Canada

Yunfeng Chen[1], Yu Jeffrey Gu[1], and Shu-Huei Hung[2]

[1]Department of Physics, University of Alberta, Edmonton, Alberta, Canada, [2]Department of Geosciences, National Taiwan University, Taipei, Taiwan

Abstract The Western Canada Sedimentary Basin marks a boundary zone between the Precambrian North American craton and the Phanerozoic Cordillera. Its crystalline basement has documented more than 3 billion years of evolution history of western Laurentia. Here we conduct a high-resolution survey of the mantle *P* and *S* wave velocities using finite-frequency tomography. Our models show pronounced eastward increases of 4% *P* and 6% *S* wave velocities beneath the foreland region, which define a sharp seismic Cordillera-Craton boundary. In the cratonic region, distinctive high- (>2%) velocity anomalies representing depleted mantle lithospheres are well correlated with major Precambrian crustal domains. The largest lithosphere thickness contrast coincides with the Snowbird Tectonic Zone, where the Hearne province extends down to ~300 km, nearly 100 km deeper than the Proterozoic terranes in northern Alberta. In the latter region, a pronounced cylindrical negative velocity anomaly extends subvertically from 75 to ~300-km depth, which potentially results from significant tectonothermal modifications during subduction and/or plume activities. At the basin scale, mantle velocities show no apparent correlations with surface heat flux, suggesting a minimum mantle contribution to the regional thermal variability. Furthermore, the long-wavelength isostatic gravity correlates negatively with the velocities, which confirms that the melt extraction from Precambrian cratons is responsible for the formation of highly depleted mantle lithospheres. Moreover, our model reveals the increased concentrations of kimberlites and lamproites near the zones of high horizontal velocity gradients. The distinct spatial pattern may reflect either preferential formation or eruption of potentially diamondiferous rocks at lithospheric weak zones near the western margin of Laurentia.

1. Introduction

1.1. Overview

Continental cratons are coherent and rigid blocks that have been relatively stable for billions of years (Griffin et al., 2003; Jordan, 1978; Sleep, 2005). Their stabilities are largely attributed to the presence of a thick depleted chemical boundary layer that counteracts the negative buoyancy resulting from thermal contraction (Griffin et al., 2003; Jordan, 1988; Lee et al., 2011). The physical and chemical differences between this coherent layer and the underlying weak, potentially water/melt-rich, asthenosphere (Fischer et al., 2010) manifest into distinctive rheological stratifications in the upper mantle (Karato & Wu, 1993; Gung et al., 2003). One of the best known examples is the North American continent, which consists of an ancient core of the Canadian Shield bounded to the west by the tectonically young Cordilleran orogenic belts. The transition region between these two tectonic domains in Canada is buried beneath the Western Canada Sedimentary Basin (WCSB), a foreland area consisting of Phanerozoic (Williston and Alberta) basins and the easternmost Canadian Cordillera (Price, 1994; Figure 1). The geographic extent of the WCSB extends from the boundary between the Omineca and Intermontane Belts to the Phanerozoic edge in the east. Its northern limit is defined by the Tathlina high, a Precambrian arch in the Slave province, and the southern boundary coincides with the Canada-U.S. border for mapping convenience (Wright et al., 1994; see Figure 1). Buried beneath the thick Phanerozoic sediment sequence, the Precambrian basement of the WCSB has recorded more than 3 billion years of the tectonic evolution history of the North American craton, highlighted by a major period of plate convergence and terrane assembly between 2.0 and 1.8 Ga (Hoffman, 1988) and a later-stage Mesozoic Cordilleran orogeny along its western margin.

Geophysical data have inferred a mosaic of domain structures in the basement of the WCSB. Among them, potential fields (gravity and aeromagnetic) provide a first-order delineation of the crustal signatures (Figure 2a), which feature Archean crustal blocks welded along major Proterozoic sutures (Figure 2b) and

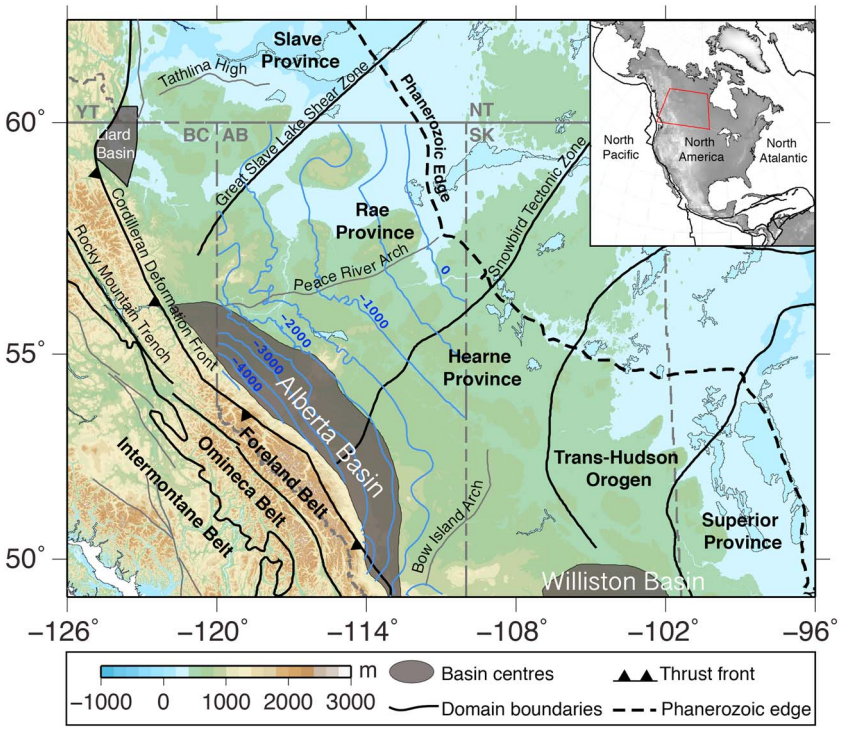

Figure 1. Tectonic map of the WCSB. Major domain boundaries are shown by the black solid lines. The Phanerozoic edge is marked by the dashed line. The three topographic highs, Bow Island, Peace River Arches, and Tathlina high, in the WCSB are indicated by the thin gray lines. The gray shaded regions indicate the deposition centers of the basins (Price, 1994). The Phanerozoic isopach (depth from the surface to the Precambrian basement) of the Alberta Basin is indicated by the blue contours. The enclosed area in the inset marks the location of the study region relative to North America.

magmatic belts (e.g., Rimbey and Taltson; Ross et al., 1991). Characterized by banded aeromagnetic signatures due to the presence of magnetite (see Figure 2a), collisional zones have preserved the protracted deformation histories of the bounding domains during the tectonic assembly of western Laurentia (Ross, 2002a). Within this tectonic framework, more detailed configuration of the Precambrian lithosphere of the WCSB was examined by seismic reflection and refraction surveys in Alberta (Ross, 2002b), an integral component of the Canadian geoscience initiative of the LITHOPROBE project (Clowes, 2010). These studies have revealed syncollisional to postcollisional structures across the inferred sutures, which are consistent with a convergent tectonic environment in the Proterozoic era (Hoffman, 1989; see Ross, 2002a for a detailed review). A synthesis of the crustal seismic observations (Lucas et al., 1993; Ross et al., 1995) and mantle electrical conductivity (Boerner et al., 1995, 1999) has led to the development of a *tectonic vise* model (Ross et al., 2000), which features contemporaneous subduction beneath the Hearne province along the Snowbird Tectonic Zone (STZ) and the Trans-Hudson Orogen (THO; see Figure 2b).

Compared with well-mapped crustal structures, the depth sensitivity to subcrustal mantle lithosphere is limited due to the primary data constraints from active source seismics. On the other hand, passive seismic surveys provide effective tools with greater penetrating powers to probe the deeper Earth structures. Earlier tomographic studies offered a glimpse of complex mantle architectures of the WCSB at continental (Frederiksen et al., 2001) and regional scales (Frederiksen et al., 1998; Shragge et al., 2002). The establishments of seismic arrays enable a more detailed examination of regional mantle lithosphere structures. One notable example is the Canadian Northwest Experiment, a 2-year (2003–2005) deployment covering much of the central-northern WCSB. The high-quality broadband data led to fruitful scientific outcomes including the discovery of fossil subduction beneath the Slave province (Mercier et al., 2008) and the detection of systematic seismic anisotropy (Courtier et al., 2010) and velocity variations (Dalton et al., 2011; Mercier et al., 2009; McLellan et al., 2018) across the Northern Cordilleran Deformation Front. During the past 10 years, the central-southern WCSB has witnessed a period of rapid expansion of broadband seismic networks, which opens a new chapter for the seismic imaging of the WCSB. Recent studies based on passive source data from

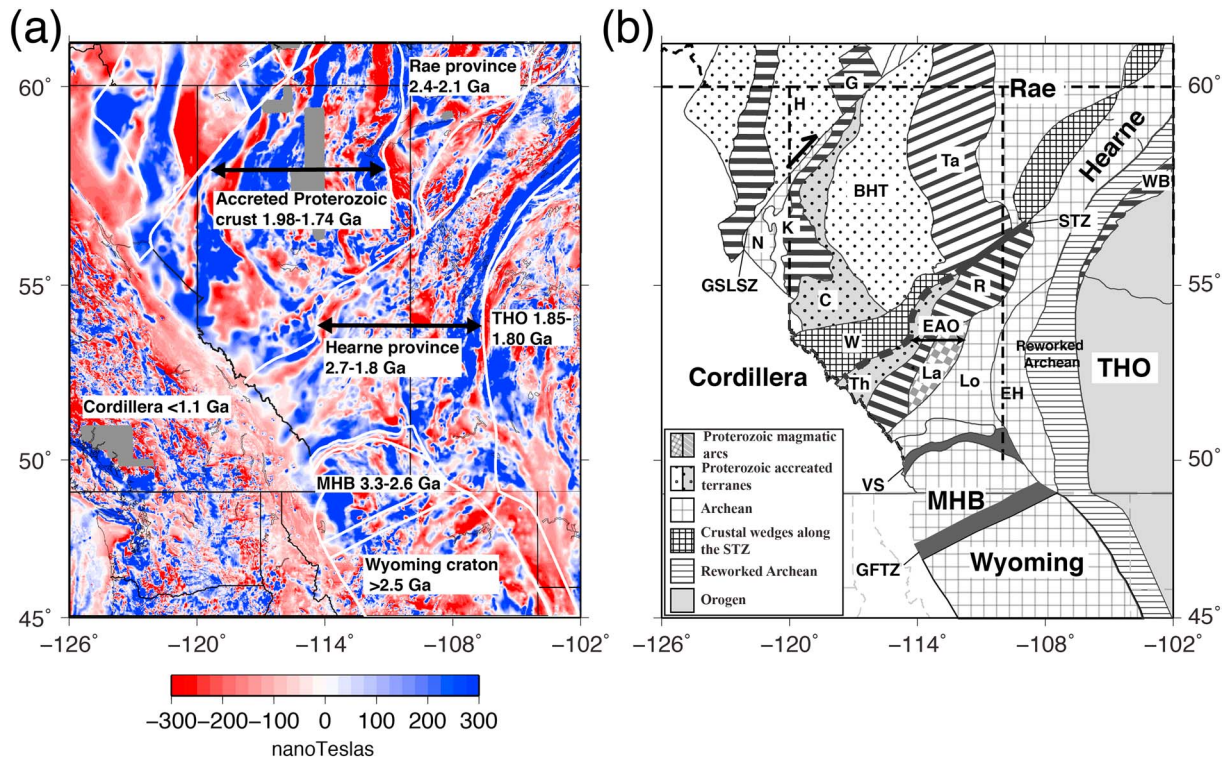

Figure 2. (a) Aeromagnetic anomaly map of the WCSB (modified after Ross, 2002a). (b) Tectonic domains of the Precambrian basement. The domain boundaries are determined based on the lineations of aeromagnetic anomalies. Major tectonic boundaries are marked by thick gray lines. Abbreviations: BHT, Buffalo Head Terrane; C, Chinchaga; CDF, Cordilleran Deformation Front; EAO, East Alberta Orogen; EH, Eyehill High; G, Great Bear; GSLSZ, Great Slave Lake Shear Zone; H, Hottah; K, Ksituan; La, Lacombe; Lo, Loverna Block; MHB, Medicine Hat Block; N, Nova; R, Rimbey; STZ, Snowbird Tectonic Zone; Ta, Taltson magmatic zone; Th, Thorsby; THO, Trans-Hudson Orogen; VS, Vulcan Structure; W, Wabamun. Modified after Ross et al. (1991).

these newly deployed arrays have unraveled complex evolution history of mantle lithosphere beneath the Precambrian crustal domains (Bao & Eaton, 2015; Bao et al., 2016; Chen et al., 2015, 2017; Gu & Shen, 2015; Gu et al., 2015, 2018). The improved structural knowledge from these earlier works and the proliferation (10+ years) of seismic data laid a solid foundation for more accurate, higher-resolution imaging of this region.

In this study, we conduct a new seismic survey of the upper mantle structures using the most updated body wave traveltime data. The resulting high-resolution mantle images from the new *P* velocity and the first finite-frequency *S* velocity models reveal small-scale seismic anomalies that are absent in previous regional-/continental-scale tomographic models. Our study is based on an integrated analysis that combines seismic velocities with constraints from heat flow, gravity, and kimberlite data, which is highlighted by (1) an accurate determination of the location of major tectonic boundaries and the surrounding mantle lithosphere structures, (2) a systematic examination of the properties (density, velocity, and inferred composition) of Archean craton(s), and (3) new evidence on the potential link between mantle velocity gradients and diamond-bearing kimberlites in northern Alberta, an undersampled region by preexisting geophysical data. These results lend new insight into the Precambrian assembly and later Proterozoic, possibly Mesozoic, modifications of western Laurentia.

1.2. Regional Tectonics

The WCSB is a foreland basin subsided in response to the load of easterly thrust sheet during the Cordilleran orogeny (Beaumont, 1981; Cant & Stockmal, 1989). The largest deposition center (i.e., the Alberta Basin) is characterized by a northeast tapering sedimentary wedge in front of the Cordilleran Deformation Front (CDF), which contains deposits from two major episodes: (1) older (Paleozoic) platformal sequences from a rifted margin and (2) younger (Mesozoic-Cenozoic) deposits from the foreland basin stage (Porter et al., 1982; Price, 1994). The sediments reach the maximum thickness of ~6 km at foothills and decrease toward the northeast leading to the exposed Canadian Shield (see Figure 1). The underlying crystalline basement

is composed of Precambrian igneous rocks of 2.7–1.8 Ga based on the U-Pb age from drill core samples (Ross et al., 1991; Villeneuve et al., 1993).

The major Precambrian domains in the study area encompass the Archean Hearne province and Proterozoic accreted terranes separated by the STZ, a proposed Proterozoic collisional suture of the western Churchill province (Hoffman, 1988; Ross et al., 1991). In central Alberta, the East Alberta Orogen, a proposed Proterozoic orogenic belt consisted of the STZ, Thorsby, Rimbey, and Lacombe domains (see Figure 2b), marks a transition region from the underlying Paleoproterozoic crust to the Archean basement of the Hearne province farther south (Ross et al., 1995, 2000). The Loverna Block, the core of the Archean Hearne province, is characterized by near-neutral aeromagnetic anomalies that are superimposed by short-wavelength positive perturbations (see Figure 2a; Ross et al., 1991). Sparsely sampled drill cores, which mainly contain magnetite-bearing biotite granite and granitic gneiss with a dominant Archean origin (2.71 Ga), have been subjected to local thermal overprinting circa 1.82 and 1.78 Ga (Villeneuve et al., 1993).

The Rimbey domain to the northwest of the Loverna Block is a magmatic belt of Paleoproterozoic era (1856–1798 Ma; Villeneuve et al., 1993), presumed to have formed in association with southeastward (current geographic location) subduction of the oceanic basin of the Thorsby domain (Ross et al., 1991). Sandwiched between the Archean Loverna Block and Proterozoic Rimbey domain is the Lacombe domain, which consists largely of low-grade clastic metasedimentary and felsic metavolcanic rocks ($<$2.3 Ga; Villeneuve et al., 1993) deposited in either a foreland-foredeep system or a marginal/intra-arc basin flanking the Rimbey arc (Ross et al., 2000). Wabamun domain northwest of the STZ is an aeromagnetic high with 2.4–2.0-Ga old magmatic rocks (Ross et al., 1991). The nature of this domain is poorly known (Boerner et al., 2000) and has been linked to a tectonic escape wedge formed during collisions along the STZ (Ross, 2002a). Our study will provide new insight into the evolution of the Wabamun domain in section 4.2.

The vast regions to the north of the STZ comprise a series of north trending aeromagnetic anomalies in possible connection with the accreted terranes in the Rae province (Ross & Eaton, 2002; see Figure 2). Among the notable domains, the Taltson magmatic zone (2.02–1.91 Ga) constitutes the southern segment of the 2,500 km Taltson-Thelon orogen (Hoffman, 1988, 1989) and contains lithologically diverse rock types of granitoids, metasedimentary gneisses, granitic basement gneisses, and amphibolites (Chacko et al., 2000). The origin of Taltson has been debated, either as a product of eastward subduction of oceanic crust beneath a continental margin (McDonough et al., 2000; Ross et al., 1991; Ross & Eaton, 2002) or, alternatively, as a distant hinterland of a convergent plate margin in a continent-interior setting (Chacko et al., 2000; De et al., 2000). To the west of the Taltson, Buffalo Head Terrane (BHT) and Chinchaga domain form the core of the Proterozoic accreted terranes. The southern BHT is intersected by the Peace River Arch (see Figure 1), a lineament of topographic high that has been active since the Proterozoic (Eaton et al., 1999). Mafic sills emplaced from postcollisional magmatism were discovered in the nearby upper crust (Ross & Eaton, 1997; Welford & Clowes, 2006). The center of the BHT was intruded by the Buffalo Hills kimberlites between 88 and 86 Ma (Aulbach et al., 2004; Banaset al., 2007; Carlson et al., 1999; Davies et al., 2004; Heaman et al., 2004).

Despite the earlier geological findings, the tectonic setting of the BHT remains elusive due to episodic overprinting events. The BHT was suggested to have strong chronological affinities to the Taltson magmatic zone based on the similar U-Pb ages and partially overlapped Nd isotopic compositions preserved in the gneiss complex of the Taltson and subsurface rocks of the BHT (McNicoll et al., 2000). The magmatic rocks with ages ranging from 2324 to 1990 Ma potentially document several thermal tectonic events, among which a suite of young granitic rocks (1998–1990 Ga) was linked to the intrusion into the basement rocks of the BHT during its collision with the Chinchaga domain to the west (Ross & Eaton, 2002). The drill cores from the latter region revealed mostly metaplutonic rocks with a crystallization age of 2.19–2.08 Ga (Villeneuve et al., 1993). Benefiting from improved seismic data coverage surrounding the BHT, our study sheds new light on the enigmatic tectonic history of this region.

These vastly diverse crustal domains form the basic building blocks of the WCSB, which were assembled into a rigid cratonic core of western Laurentia during a short geological period between 2.0 and 1.8 Ga (Ross et al., 1991). The cratonic interior remains relatively stable over the last 2 billion years (Schaeffer & Lebedev, 2014; Yuan & Romanowicz, 2010), whereas the western margin of Laurentia has undergone profound evolution from a miogeocline (passive margin) initiated in Late Precambrian (Stewart, 1972) or Early Paleozoic (Bond

& Kominz, 1984) to a convergent margin during the Mesozoic-Cenozoic Cordilleran orogeny (Coney, 1989; Dickinson et al., 2009; Evenchick, 2007; Johnston, 2001).

In short, our study region has recorded almost three quarters of Earth history (3.3 Ga), which provides an excellent natural laboratory for investigating the evolution of continental lithosphere dating back as to the Archean. These earlier investigations are based primarily on geochronological analyses of drill core samples and potential field observations, which establish a general tectonic framework for western Laurentia but apply mainly to the crustal depths. As a result, questions remain on (1) how these crustal subdivisions are manifested in the mantle lithosphere, (2) how these tectonic events initiated and/or modified the intrinsic stability of craton, and (3) what surface expressions (e.g., gravity, heat flow, and discoveries of kimberlites) are attributable to mantle dynamics. Answers to these questions are predicated on improved imaging, and proper integration, of mantle *P* and *S* wave speeds beneath the WCSB, which are the overarching objectives of this study.

2. Data and Method

2.1. Station and Earthquake Distributions

Earthquake data used in this study are recorded at 89 broadband stations from five regional networks near the WCSB (Figure 3a). Among them, the Canadian Rockies and Alberta Network (CRANE; since 2006; Gu et al., 2011) and Regional Alberta Observatory for Earthquakes Studies Network (RAVEN; since 2013; Schultz & Stern, 2015) offer the primary constraints on northern and central WCSB, whereas the Transportable Array (TA) component of USArray (2006–2009; partially overlapped with the initial CRANE deployment) greatly improves the data coverage in the southern WCSB (see Figure 3a). Also included are 26 stations from CANOE (2003–2005) for resolution improvement near the northern Canadian Rockies. Our data set comprises *P* and *S* wave traveltimes from teleseismic events (28–95°) with a minimum magnitude of 5.5. The earthquake epicenters (1,729 and 1,263 for *P* and *S* wave analyses, respectively) are populated along the northwestern and eastern Pacific subduction zones (Figure 3b).

2.2. Teleseismic Traveltime Data

The traveltimes of body waves are frequency dependent due to intrinsic propagation effects such as diffraction scattering and wavefront healing (Dahlen et al., 2000; Hung et al., 2000). To account for the frequency dependence of traveltimes, we filter the seismic signals into multiple bandwidths by applying a third-order band-pass Butterworth filter with frequency ranges of 0.03–0.125 Hz (low) and 0.3–2.0 Hz (high) for *P* waves on the vertical component and 0.03–0.1 Hz (low) and 0.1–0.2 Hz (high) for *S* waves on the tangential component. The *P* wave frequency range is carefully determined to minimize the effect of a noise peak at ~0.2 Hz (supporting information Figure S1). Traveltimes are measured at all stations recording the same teleseismic event. Preliminary traveltimes of *P* and *S* phases are predicted based on AK135 (Kennett et al., 1995), a 1-D reference continental Earth model; at this stage, heterogeneities become apparent from the misalignment of the arrivals (Figure 4a). We then measure the time shifts between station pairs using the Multi-Channel Cross-Correlation method (MCCC; VanDecar & Crosson, 1990; Figures 4b–4c). This method determines the relative delay between each station pair (Δt_{ij}) as the time shift that leads to the maximum cross-correlation value. Consequently, the group of N observations results in $N(N-1)/2$ relative traveltime measurements, which forms a system of linear equations as follows:

$$t_i - t_j = \Delta t_{ij}, \tag{1}$$

where t_i and t_j are traveltimes at the ith and jth stations, respectively. Further least squares optimization is applied to this inverse problem as well as a constraint of $\sum t_i = 0$ to minimize the inconsistency of traveltimes across the array due to data noise or measurement uncertainties. This additional constraint term removes the average, which effectively minimizes the traveltime uncertainties associated with the source effects (location and origin time). This process also eliminates the absolute velocity of the model and results in perturbations relative to an unknown regional mean. The final relative traveltime residuals are defined by subtracting the demeaned (i.e., average-removed) theoretical (AK135-predicted) arrival times from the cross-correlation-based values. The final refined data set contains 23,123 and 17,253 high-quality *P* and *S* measurements, respectively.

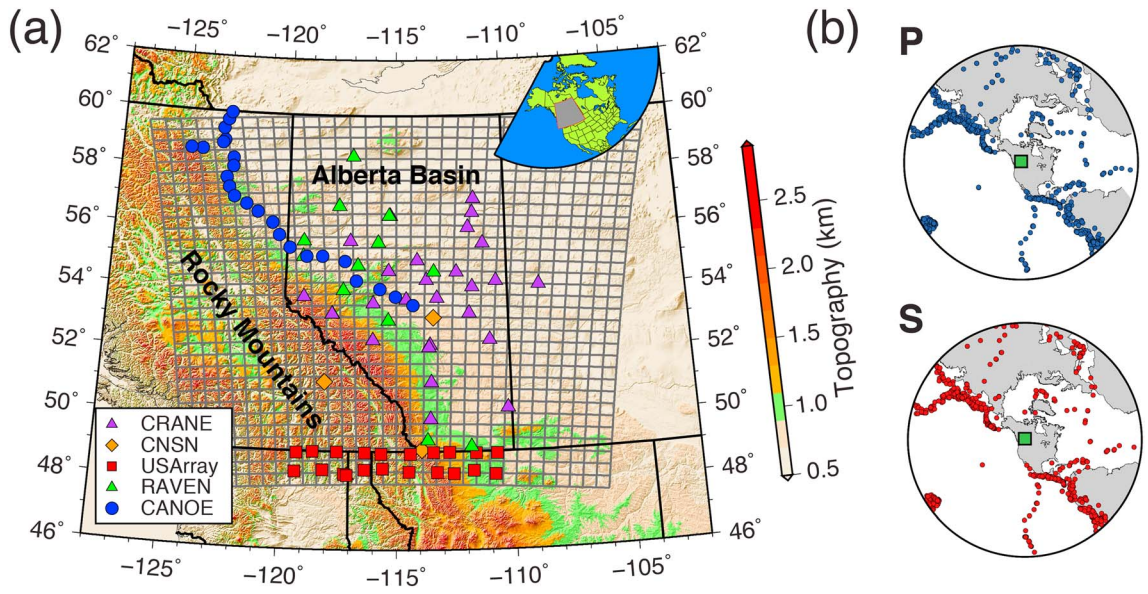

Figure 3. (a) Seismic stations used in this study. Stations from five different networks are marked by the various symbols superimposed on the surface topographic relief. The gray lines outline the mesh used in the tomographic inversions. The study region is shaded in gray in the map inset. (b) Earthquake distributions of *P* and *S* wave data. The circles mark the epicenters, and the green square indicates our region of study.

Teleseismic body waves incident nearly vertically beneath a recording array, which results in poor vertical resolutions at shallow (especially crustal) depths. Consequently, crustal velocities and depth could be incorrectly mapped into the underlying mantle (Hung et al., 2004). To mitigate this problem, we use time shifts to correct for uneven Moho depths, which are crucial for regions such as the WCSB where the crust thickens by as much as 15 km from the Cordillera to the Rocky Mountain foothills (Gu et al., 2018). To account for lateral variations in both crustal depth and velocity, we trace rays through CRUST1.0 (Laske et al., 2013), a 1 × 1° global crust model, to the surface while assuming a fixed geometrical path predicted from AK135 reference model. The difference in the crustal traveltime between CRUST1.0 and AK135 models is then used as the crustal correction term that is subsequently removed from the relative traveltime residuals. The correction contributes to as much as ~0.6 and ~1.1-s traveltime perturbations for the respective *P* and *S* wave measurements across the seismic array (supporting information Figure S2). The model choice and approximation are prompted by the lack of published regional studies of crustal velocity and thickness, especially for *P* waves that are critical for this study. The accuracy of CRUST1.0 is verified by a recent receiver function analysis of the Alberta Basin (Gu et al., 2018). We also compute the *S* wave crustal correction values for stations in central-southern Alberta based on a regional shear velocity model (Gu & Shen, 2015), which was derived using a subset of the stations and recordings adopted in this study. The resulting correction values only differ by 0.15 s on average compared with those from CRUST1.0, which results in ~11% change in the relative traveltime residual (supporting information Figure S3). The final traveltime pattern remains largely unchanged for the cratonic region, the main focus of this study. As the final step, topographic corrections are applied in the form of additional time shifts to compensate for large surface elevation variations in the study region. The corrected differential traveltimes show consistent variations between *P* and *S* waves but differ in strength: *P* wave variations account for about 40% of the *S* counterparts (Figure 5). The traveltime pattern could visually be subdivided into two distinctive halves, a positive (time delay) Cordillera and a negative (time advance) craton separated roughly by the CDF, and suggests large structural variations across the study region.

2.3. Finite-Frequency Tomography

The corrected relative traveltime residuals are subsequently used in the inversions of mantle velocity structures. We adopt the finite-frequency method, which considers the volumetric, rather than linear, model sensitivity along the geometrical raypath (Figure 4d). The finite-frequency theory (Dahlen et al., 2000; Hung et al., 2000), the basis of our tomographic inversion, relates an observed traveltime measurement to model parameters (slowness) through the following equation:

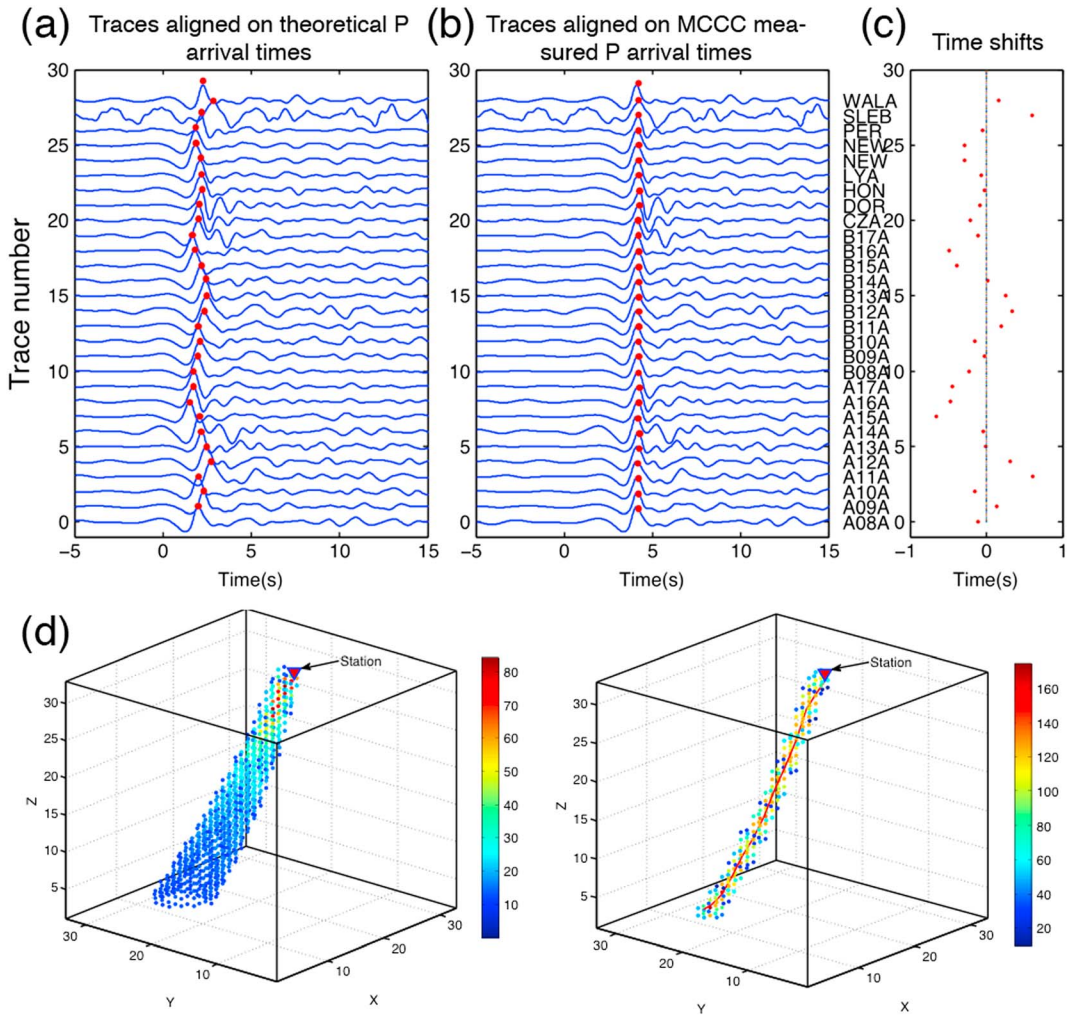

Figure 4. Sample traveltime measurements for an event recorded at the seismic array. The seismic traces are aligned on the (a) theoretical and (b) MCCC optimized *P* wave arrival times. The red circles mark the peaks of *P* phases. (c) Time shifts relative to the average traveltime of all recording stations for this event. (d) Station-side inversion kernels derived from finite-frequency (left) and traditional ray (right) theories, constructed using high-frequency *P* wave measurements for a teleseismic earthquake at an epicenter distance of 85°. The finite-frequency kernel provides the varying volumetric wave sensitivity to slowness perturbations surrounding the propagating raypath. Contrary to a constant sensitivity predicted from ray theory, the sensitivity (amplitude) of finite-frequency kernel scales inversely with the size of the Fresnel zone.

$$\delta t = \iiint_{\oplus} K(\mathbf{x})\delta s(\mathbf{x}) d^3\mathbf{x}, \tag{2}$$

where $K(\mathbf{x})$ is the Fréchet derivative (i.e., sensitivity kernel) that maps the slowness perturbation δs at a point $\mathbf{x}$ within in model volume $\oplus$ to relative traveltime residual δt. The kernel is computed using the Born forward scattering theory in combination with a paraxial ray approximation (Dahlen et al., 2000; Hung et al., 2000), which properly considers the effects of wavefront healing and diffraction scattering on seismic wave propagation (and hence traveltime shifts). We parameterize our region of study into a spherical grid covering an area of 12 × 12° and extending 800 km in depth. We assign 33 nodes along each direction, which translate into a semiuniform (spherical) grid size of about 40, 40, and 25 km in latitude, longitude, and depth, respectively (see Figure 2). The model parameters can be solved by formulating equation (2) into a concise matrix form

$$\mathbf{d} = \mathbf{G}\mathbf{m}, \tag{3}$$

where $\mathbf{d}$ is the data vector contains M (23,123 for *P* and 17,253 for *S*) relative traveltime residuals and $\mathbf{m}$ is the

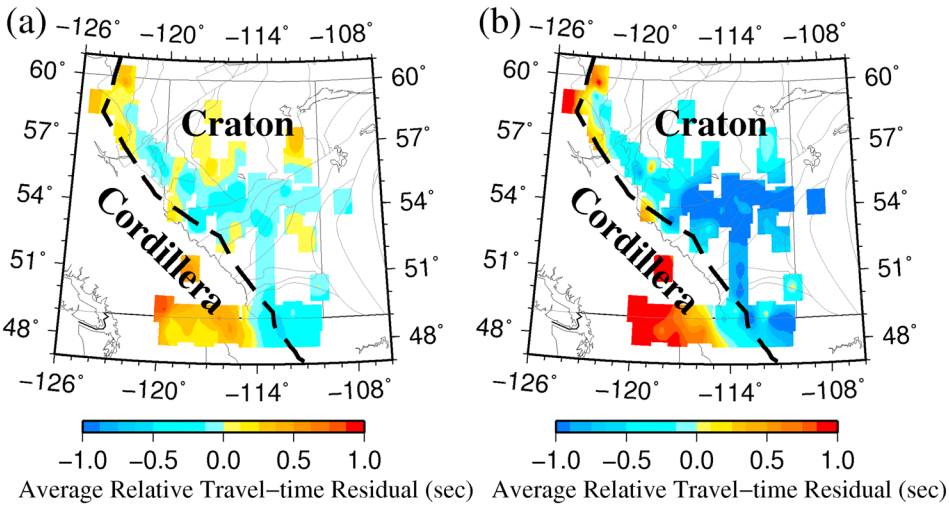

Figure 5. Color-coded (a) *P* wave and (b) *S* wave average relative traveltime residual at each station after minor spatial interpolation. Positive and negative values represent time delay and advance, respectively, relative to the regional mean. The dashed line marks the Cordilleran Deformation Front.

model vector that contains N ($33 \times 33 \times 33 = 35{,}937$) slowness values. The corresponding inversion kernel **G** is then a M × N matrix that defines the sensitivity of the datum (**d**) to a slowness perturbation (**m**). Instead of solving equation (3) directly in a grid-based parameterization, we recover *P* and *S* velocities independently and transform the model vector and inversion kernel to the wavelet domain. We then seek a damped least squares solution for wavelet coefficients corresponding to each wavelet basis (i.e., hierarchical scale). This approach takes advantage of a data-adaptive scheme of nonstationary regularization and enables spatially varying resolution in the resulting model. More details on finite-frequency theory and multiscale parameterization can be found in Hung et al. (2011).

3. Result

3.1. Resolution Test

To avoid overinterpreting the outcomes of the inversions, we first examine the spatial resolution of our model using a *checkerboard* test. To do so, an input model is constructed with alternating velocity perturbations with amplitudes of 3% and 5% for *P* and *S* wave models, respectively. The checker sizes vary between 5 and 7 nodes, corresponding to a lateral dimension of 150–250 km, to investigate the resolving power of our data (Figure 6). Synthetic data (relative traveltime residuals) are computed using the actual station-event geometries with added Gaussian noise that is comparable to the observed traveltime standard deviations (0.05 s for *P* model and 0.16 s for *S* model). An inversion is then performed by adopting the same parameterization (wavelet transform) and damping schemes as those of the actual data.

The mantle checkerboard anomalies are successfully recovered in the southern half (below 55°N) of the models in all test cases (Figure 6a). The highest nominal spatial resolution is observed in central-southern Alberta and southwestern British Columbia (BC) at depths greater than 150 km, where velocity anomalies with lateral and vertical dimensions of ~100 km are robustly resolved. The well-constrained model space directly contributes to the determination and analysis of the cratonic structures in the southern WCSB. The smearing becomes more severe toward the northern corners of the model due to reduced ray coverage (see Figures 6a), where anomalies smaller than ~200 km cannot be robustly resolved (see recovered models near 250-km depth in Figure 6a). The location of vertical boundaries between *checkers* with alternating signs are accurately recovered in the southernmost Alberta (see cross-section AA′ in Figure 6b) as a consequence of higher lateral sensitivity of teleseismic body waves, which provides ideal resolution to constrain the Cordillera-Craton boundary, a key imaging target in this study. The corresponding *S* resolution test results suggest a minimum resolvable scale of ~200 km laterally, which is sufficient for imaging

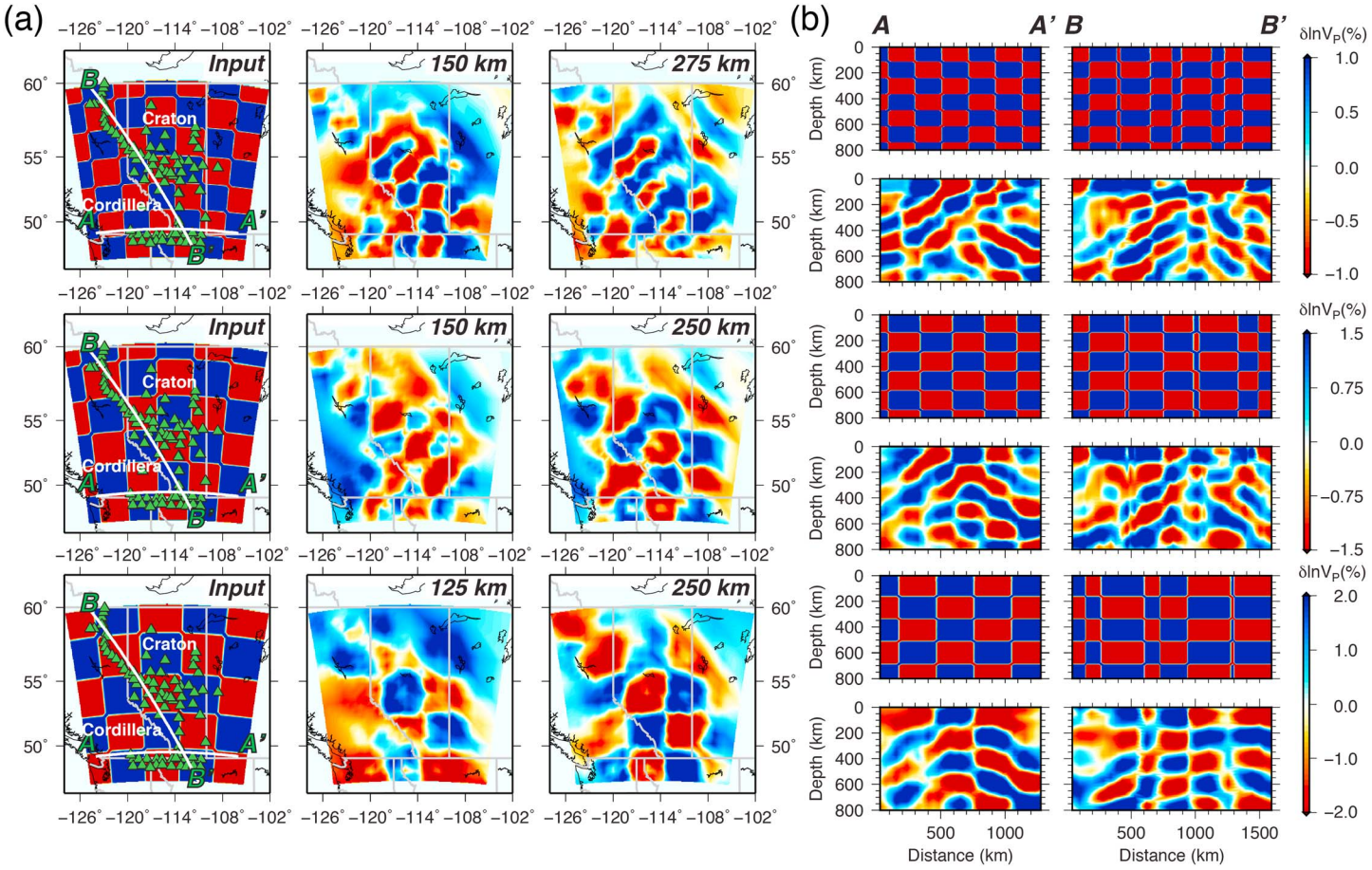

Figure 6. Checkerboard resolution test using various anomaly sizes. (a) Input *P* wave velocities (left panel) and the recovered pattern near 150 km (middle panel) and 250 km (right panel) depths. The green triangles indicate the seismic stations. (b) The corresponding checkerboard test results along two cross-sections marked by the white lines in the input model.

major seismic anomalies (e.g., deep craton root and large-scale Cordillera-Craton boundary) in this region (supporting information Figure S4).

3.2. *P* and *S* Velocity Models

P and *S* wave tomographic models reveal consistent mantle velocity variations across the region of study. The dichotomy of velocities is apparent as negative velocities dominate the upper mantle beneath the Canadian Cordillera and positive velocities underlie much of the Precambrian basement of the WCSB (Figure 7). In the west, *P* (*S*) wave velocity perturbations of −2% (−3%) reside above 250-km depth and the amplitudes gradually decrease at greater depths. In the east, high velocities with a maximum amplitude of 2% for *P* wave (3% for *S* wave) extend down to at least 150 km (e.g., region 1 in Figure 7a). The transition region is characterized by 4% *P* and 6% *S* velocity increases toward the craton, which forms a sharp velocity boundary in the Foreland Belt (see Figure 1 for location) parallel to the CDF. The high velocities on the craton side are interspersed with zones of below-average velocities. A broad low-velocity zone is observed above 150-km depth in southern Alberta, which is spatially confined within the boundaries of the Hearne province (see Figures 7a and 7b). The most pronounced low-velocity zone is observed in northern Alberta (region 2 in Figure 7a), showing a maximum (negative) velocity amplitude of 2–3%. This anomaly emerges at 75-km depth and extends subvertically downward to ~300 km, where its amplitude reduces and equilibrates with the surrounding mantle. This vertically elongated low-velocity zone is truncated in the south by a deep-seated high-velocity structure beneath the Hearne province (see region 3 in Figure 7d). The transition from low to high velocities spatially coincides with the STZ, an important structural boundary in the western Churchill province (Hoffman, 1988). Its significance on regional tectonics will be discussed in section 4.2.

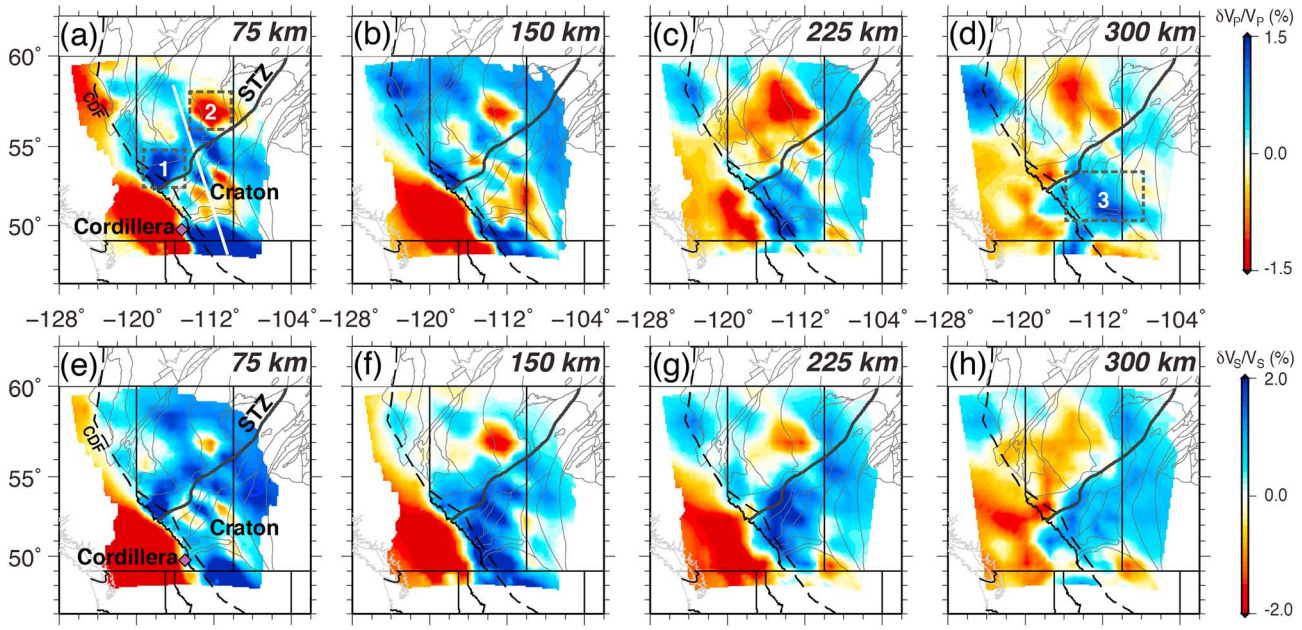

Figure 7. (a–d) *P* and (e–h) *S* wave tomographic models between 75 and 300-km depth. The numbers (1–3) label the key structures discussed in this study. Regions with less data sampling are masked. The dashed line marks the CDF, which approximately divides the low velocities in the west from the high velocities in the east. The white line indicates the location of the profile shown in Figure 11. Kimberlite intrusion site sampling the southwestern Hearne province is marked by the purple diamond at 75 km (Canil et al., 2003).

3.3. Model Comparisons

Our model is constructed from the most up-to-date regional broadband data set, which offers substantially improved model resolution compared with the earlier tomographic models. We compare our models with six recent regional-/continental-scale models. The most relevant comparisons are made with regional *P* and *S* velocity models of the upper mantle in western Canada (Mercier et al., 2009; M09P and M09S; Figure 8), which are inverted using the ray-theoretical kernel from 23,420 *P* wave and 15,805 *S* wave delay times, respectively. The large-scale velocity structures and local anomaly distributions are consistent between model M09 and our model in the upper mantle, despite vastly different data sets and inversion kernels (ray versus finite-frequency; see Figure 4d). For example, both models reveal a sharp transition from low-velocity Cordillera to high-velocity cratons across the CDF, as well as a high-velocity zone beneath the foothills of the Canadian Rockies in southern Alberta. Similar to the reduced velocities beneath northern Alberta observed in our *S* model, M09 (*S*) also shows negative perturbations throughout the upper mantle to the north of the STZ.

Further comparisons with our models are made with three continental-scale shear velocity models: (1) the NA07 (Bedle & van der Lee, 2009) constructed from 5,549 vertical waveforms, (2) SL2013NA (Schaeffer & Lebedev, 2014) computed using 717,000 vertical-component seismograms, and (3) a more recent North America model (NA14; Yuan et al., 2014; see Figure 8) inverted from 1,050,000 Rayleigh and Love wave fundamental and overtone waveforms. All three models show similar low-to-high-velocity transition as those observed in our study, despite limited short-wavelength velocity variations due to relatively coarse model parameterization and low-frequency surface waves used in their inversions. It is worth noting that NA14 (Yuan et al.,2014), the most recent continental-scale model of North America in our analyses, shows a zone of reduced wave speeds in northern Alberta, similar to our model observations.

We correlate our seismic velocities with those in other models at lithospheric depths for quantitative comparisons (Figure 9). To ensure a comparable model resolution, we filter all body wave models to the wavelength of surface waves using a 2-D Butterworth low-pass filter with corner wave numbers of 300 km, considering typical wavelengths of 200–1,000 km for 50–160-s period surface waves (Lebedev & Nolet, 2003). Despite the independent data constraints, our *P* and *S* models are self-consistent and exhibit an average correlation coefficient of ~0.8 at depths shallower than 200 km. The correlation coefficients with three recent continental-scale models are comparable with the *autocorrelation* (i.e., correlation between our *P* and *S* models) results

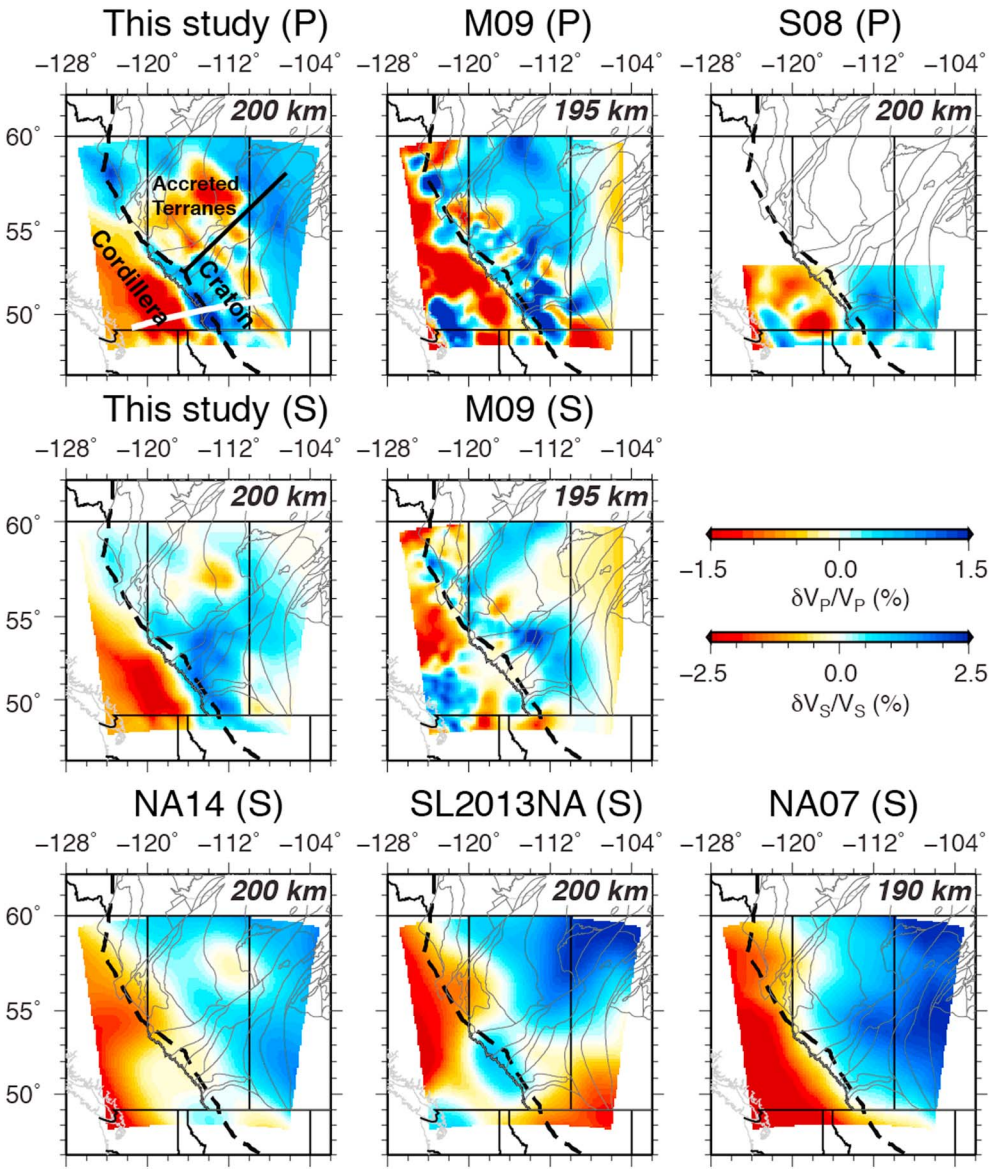

Figure 8. A comparison of models from this study with six recent tomographic models near 200-km depth, which includes M09 (Mercier et al., 2009), S08 (Sigloch et al., 2008), SL2013NA (Schaeffer & Lebedev, 2014), NA07 (Bedle & van der Lee, 2009), and NA14 (Yuan et al., 2014). The dashed line marks the Cordilleran Deformation Front. In the *P* wave model of this study, the black solid line approximates the boundary between the Hearne craton in the south and accreted terranes in the north and the white line indicates the profile from the Cordillera to craton shown in Figure 10.

above 150-km depth, suggesting a similar first-order structural variation in all models. The coefficients decrease gradually in the depth range of 150–200 km and fall off sharply below 200 km. On the other hand, the correlation with the body wave model (S08; Sigloch et al.,2008) is relatively high (~0.6) in the depth range of 100–200 km without a significant downward decrease. Overall, the correlation coefficients of all models are within one standard deviation (0.2) of the mean (0.6) at depths above 200 km except for M09S (see Figure 9). The deviation from M09S likely results from its relatively low data resolution in the cratonic region due to limited (typically less than 2 years) recording time windows of temporary seismic arrays.

4. Discussion

Compared with earlier regional-/continental-scale studies (see Figure 8), our *P* and *S* models show complex velocity variations on the western margin of Laurentia, a region cored by the Archean-aged (Hearne and

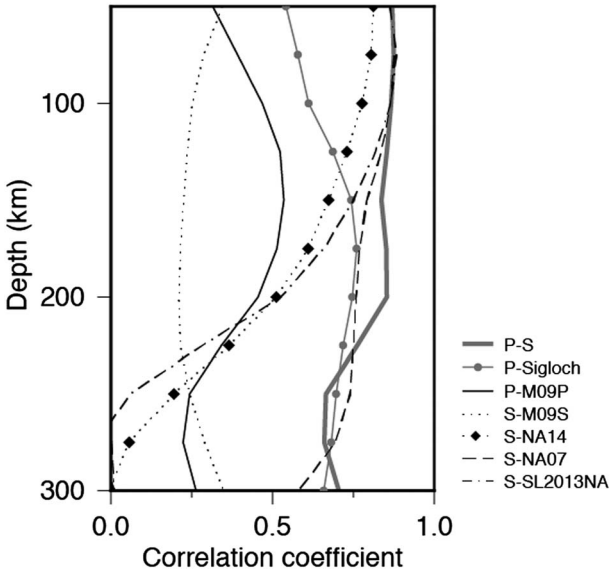

Figure 9. Velocity correlations between eight tomographic models at depths between 50 and 300 km.

MHB) cratons bounded by the Proterozoic accreted terranes to the north and the Phanerozoic Cordillera to the west. This unique tectonic setting offers a continuous sampling of the Earth history dating back to ~3 billion years ago and lends new insight into the growth and evolution of the North American continent.

4.1. Cordillera to Craton Transition

The large velocity contrast between the Cordillera and craton forms a first-order structural gradient beneath the Foreland Belt (see Figure 8). Despite the differences in the strength of velocity perturbations, all models show a unique low-to-high-velocity variation associated with the Cordillera-Craton transition. We associate the low velocity to the high-temperature mantle beneath the Cordillera and the high velocity to the mantle lithosphere beneath the cratons. The transition region is characterized by a sharp velocity gradient, which marks a seismological Cordillera-Craton boundary (CCB). Our model shows a well-defined CCB that is significantly sharper compared with the smooth gradient in other models (Figure 10), which we attribute to a better horizontal resolution offered by body waves (in comparison with surface waves) and improved data coverage from regional seismic arrays. The transition from the lowest to the highest velocities across the CCB occurs within a lateral distance of 200 km in our *P* model, and the corresponding transition length is ~300 km in the *S* model. The location of this boundary lies beneath the Foreland and Omineca Belts in the orogenic hinterland, adjacent to a prominent topographic low of the southern RMT (see Figure 10). This seismologically defined CCB coincides with a thermal boundary that separates the high heat flow of 80–100 mW/m^2 in the Cordillera from the lows of 40–60 mW/m^2 in the craton (Hyndman & Lewis, 1999). The suggested thickness of this thermal boundary is less than 200 km (Hyndman & Lewis, 1999), which agrees well with the length scale of the velocity transition in our model. At shallower depths, the crustal thickness increases abruptly from ~33 km beneath the Cordillera to ~50 km in the craton near the RMT (Clowes et al., 1995; Gu et al., 2018; Gu & Chen, 2015). These observations provide compelling geophysical evidence for the presence of a lithospheric-scale structure near the southern RMT, which likely marks a destructive (Bao et al., 2014; Levander et al., 2011) or a collision boundary between the exotic Cordillera and craton autochthon (Johnston, 2008). A notable character of the CCB is its steep westward dipping geometry as clearly defined in our model, and a similar observation has been recently reported in a surface wave model of western Canada (Zaporozan et al., 2018). This unique westward dip contradicts with an assumed landward dipping geometry of the craton margin in a back-arc setting (Hyndman et al., 2005) and could potentially represent a preserved collisional front (Johnston, 2008). Overall, our new models provide the most updated seismic constraints on the sharpness, location, and geometry of the CCB, which are critical to deciphering the nature and style of the Cordillera's orogenesis. More detailed discussions are beyond the scope of this paper and will be provided in a separate study.

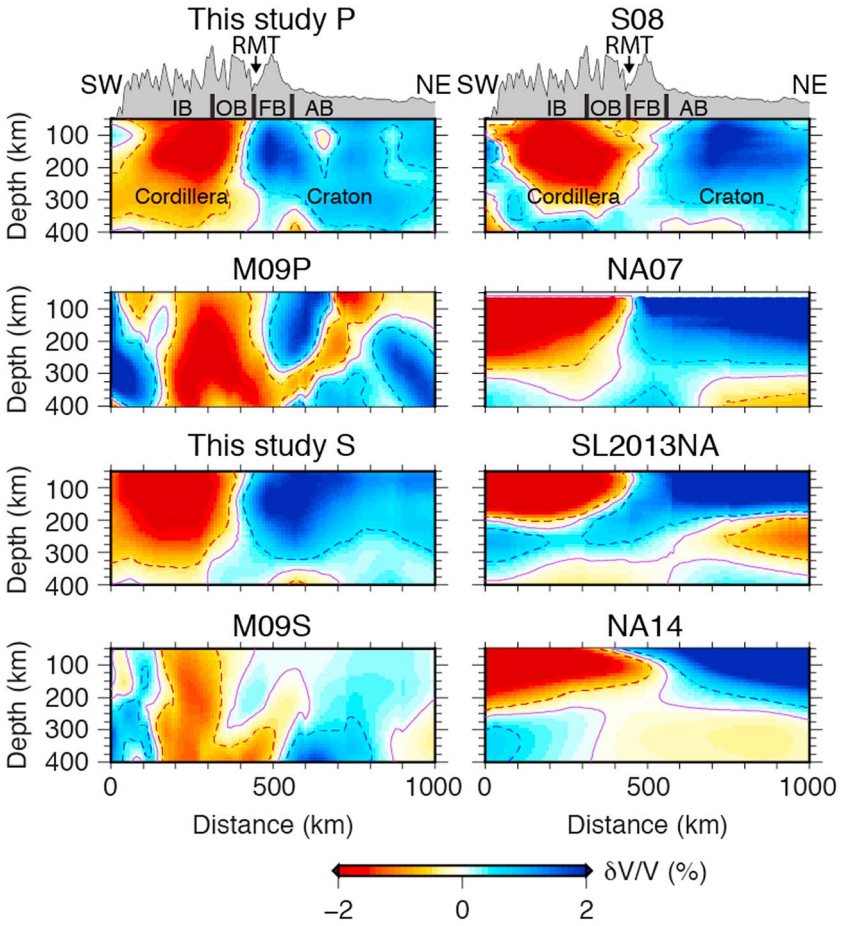

Figure 10. Cross-sections showing the Cordillera-Craton transition from this study and six recent tomographic models. The profile location is indicated by the white line in Figure 8. Abbreviations: AB, Alberta Basin; FB, Foreland Belt; OB, Omineca Belt; RMT, Rocky Mountain Trench; IB, Intermontane Belt. The red, purple, and blue lines indicate −1, 0, and 1 percent velocity contours, respectively.

4.2. Craton Structures Revealed From *P* and *S* Wave Models

Earlier seismic reflections of the Central Alberta Transect revealed crustal-scale imbrication across the Hearne province (Ross et al., 1995). Observations of a highly deformed crust (Lucas et al., 1993; Ross et al., 1995) and elevated mantle conductivity (Boerner et al., 1999) beneath the Hearne province led to the *tectonic vise* hypothesis (Ross et al., 2000), which resulted from coeval Proterozoic underthrusting along the northwestern (STZ) and southeastern (THO) margins of the Hearne province. This model further stipulates that the lithosphere of the Archean Hearne craton was thinned by either delamination due to gravitational instability or convective erosion followed by a contracted and thickened lithosphere (Ross et al., 2000), though this model was challenged by the observations of a high-velocity lithospheric root in later tomographic studies (Bao & Eaton, 2015; Chen et al., 2017; Shragge et al., 2002).

Our new *P* velocity model expands the data set in Chen et al. (2017) by including an additional 26 stations in central-northern Alberta (see Figure 3). The resulting mantle image validates the presence of a pronounced high-velocity zone in the depth range of 200–300 km beneath the Hearne province (see Figure 11a). This inferred deep lithospheric root rules out a wholesale replacement of the Hearne lithosphere following thickening during episodes of the Precambrian collisions (Chen et al., 2017). Above this deep root, the *P* wave model shows a distinctive low-velocity zone between 100 and 200-km depths (Figure 11a). The spatial distribution of this low-velocity zone is in excellent agreement with an earlier reported low-resistivity mantle at 150-km depth beneath the Hearne province (Boerner et al., 2000; Ross, 2002a). This surprisingly conductive region within the typically resistive Archean mantle was explained by (1) the remnant of a metasomatic or melt interaction event (Boerner et al., 1999), (2) metasomatic modification of the lithosphere following the

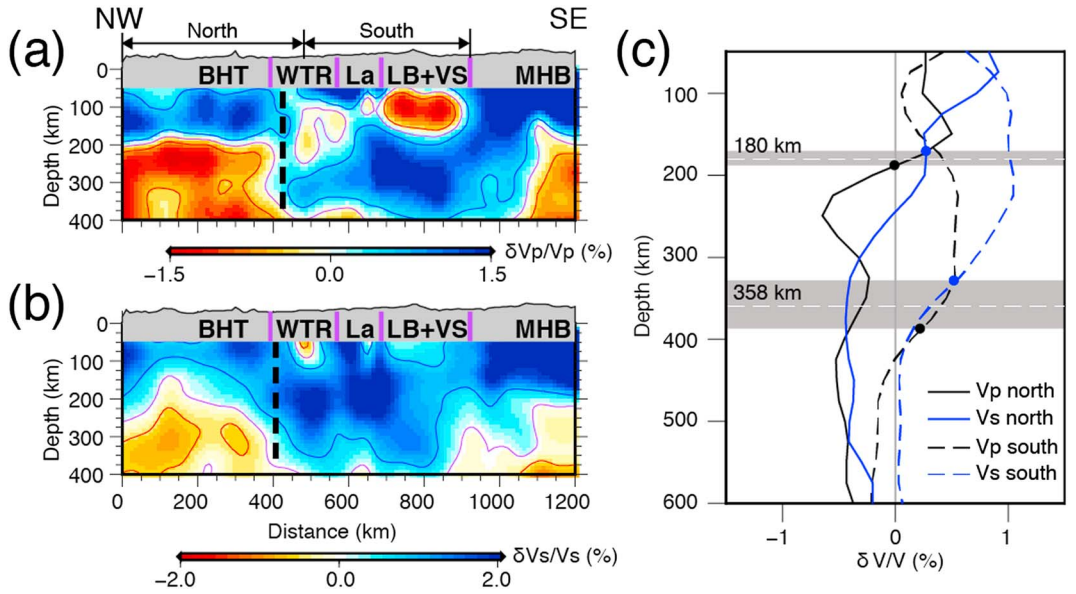

Figure 11. (a) *P* and (b) *S* wave velocities along a cross-section in the Alberta Basin. The dashed line marks the transition from thin (north) to thick (south) lithospheres across the STZ in central Alberta. The location of the cross-section is indicated by the white line in Figure 7. The red, purple, and blue lines indicate −0.5 (−0.75), 0, and 0.5 (0.75) percent *P* (*S*) velocity contours, respectively. (c) Average 1-D velocities for crustal domains to the north and south of the STZ. The circles mark the base of the lithosphere determined from the maximum velocity gradients. The shaded regions show the range of lithosphere depths from *P* and *S* models, and white dashed lines indicate the mean values.

delamination of the Hearne keel (Ross et al., 2000), (3) hydrous minerals introduced through successive episodes of subduction (Shragge et al., 2002), or (4) mantle enrichment through the subduction along the VS (Nieuwenhuis et al., 2014). Our preferred mechanism involves episodic mantle enrichment events (combination of mechanisms 3 and 4) in association with the multistage lithospheric thickening of the Hearne craton (Chen et al., 2017). Further evidence of the modification to the Archean Hearne craton was revealed by the mantle xenoliths of the garnets from the Cross kimberlite, which sampled the edge of the Hearne province in southeastern BC (see Figure 7 for location) and supported a post-Archean replacement and modification of the mantle lithosphere (Canil et al., 2003).

To first order, the *S* model shows consistent velocity variations with the *P* wave counterparts (Figure 11b). The deepest lithospheric root, as indicated by vertically coherent high velocities, is found beneath the Hearne province, and the lithosphere becomes substantially thinner (~200 km) toward the BHT and MHB. A common observation in both models is the well-defined transition from thick to thin lithospheres in central Alberta. The base of the craton is determined using a derivative based approach while assuming that the lithosphere-asthenosphere boundary marks a sharp jump in seismic velocities (Chen et al., 2017; Figure 11c). The resulting lithosphere depths in northern and southern Alberta are ~160 and ~300 km after correcting for vertical smearing in the respective regions (see Figure 6), consistent with the earlier measurement from Chen et al. (2017). The depth estimate in the latter region (Hearne craton) is about ~50 km greater than the reported value (~260 km) from surface wave tomography in the same region (Bao & Eaton, 2015). This discrepancy is likely caused by the relatively coarse depth parameterization (25-km node spacing) of our model and the limited vertical resolution of body waves (Priestley & Tilmann, 2009). Except for these seismic constraints, the geochemistry data support the presence of a thick (>200-km) lithosphere with distinctive Proterozoic characters until at least the Triassic (Canil et al., 2003). This imposes a temporal constraint on the deep Hearne root, suggesting a long-lived structure that has undergone minimal modifications since the Proterozoic, which is consistent with the proposed multistage lithospheric thickening process during the Precambrian (Chen et al., 2017). On a global scale, our measured lithosphere thicknesses (160–300 km) agree with an average value of 250 km from seismic data (Polet & Anderson, 1995) and bimodal thermal thicknesses of 200–220 and 300–350 km for Archean and early Proterozoic lithospheres (Artemieva & Mooney, 2001). Similar values are also found near the northern Hearne province in the Hudson Bay region, where the thickness of the cratonic lithosphere varies between 180 and 280 km (Darbyshire et al., 2013). Between the *P* and *S*

models, the latter shows similar decreased velocities beneath the southernmost Hearne province but less definitive horizontal mantle stratifications (e.g., associated with the lithosphere-asthenosphere boundary). This discrepancy could be partly explained by reduced model resolution due to fewer crossing raypaths (see supporting Figure S4), though spatial averaging due to lower frequency *S* waves (hence broader sensitivity kernels) could be partially responsible.

Our new high-resolution *P* and *S* models reveal previously unreported small-scale velocity anomalies that are well correlated with crustal domains. The Wabamun domain is underlain by high velocities extending to 200-km depth (see region 1 in Figure 7) and terminates sharply in the south at the STZ. The presence of a lithospheric root provides compelling geophysical evidence for the Wabamun domain as an independent microcontinent that collided with the Hearne province during the Proterozoic (Ross, 2002a). The large (>100-km) depth contrast forms a prominent lithospheric step that spatially overlaps with the STZ (see Figure 7) and, coupled with a locally depressed Moho (Bouzidi et al., 2002; Gu et al., 2018), collectively defines a collisional suture along the southern STZ in the subsurface of the WCSB.

In northern Alberta, the velocity beneath the BHT is significantly faster than the Taltson magmatic zone (see region 2 in Figure 7). These two domains were suggested to represent a single Paleoproterozoic crustal entity evolved from variable contributions of the depleted mantle (McNicoll et al., 2000). In this case, the higher velocity beneath the BHT may result from a greater extent of mantle depletion. The junction of these two domains is characterized by a pronounced low-velocity zone that extends to 300-km depth or greater. This low-velocity zone coincides with regions of increased heat flow, which may suggest potential high mantle temperatures and partially contribute to the reduced seismic velocities (Artemieva, 2006; Griffin et al., 2003). However, given a proposed conductive cooling age since 1.9 Ga of the BHT (Ross & Eaton, 2002), a more plausible explanation is the compositional modification to the depleted Archean mantle lithosphere (Aulbach et al., 2004). Both the BHT and Taltson have been suggested as the upper plates during subductions, and their crusts have been overprinted by postcollisional magmatism (Ross & Eaton, 2002). The subducted oceanic plate could have induced dehydration melting of the slab, which would effectively enrich the overlying continental lithosphere through melt percolation. A similar mechanism of subduction-driven metasomatism was invoked to explain the velocity decrease at the eastern margin of the North American craton (Boyce et al., 2016). This interpretation was supported by the mantle xenolith and xenocryst data from the Buffalo Head Hills kimberlites, which suggest that mantle has undergone at least two episodes of metasomatism by respective silicate and volatile-rich melts in the deep and shallow lithospheres (Aulbach et al., 2004). During the protracted period of melt interaction, the velocity of an originally depleted lithosphere could be reduced through (1) refertilization of the mantle lithosphere (Griffin et al., 2008; Lee et al., 2011) and (2) modification (increase) of temperature due to concentrations of radioactive elements (Artemieva, 2009; Hieronymus & Goes, 2010). This joint thermochemical effects could explain seismic anomalies up to 3–4.5% in *Vs* and 2.5–4% in *Vp* (Hieronymus & Goes, 2010), which are sufficient to explain the observed low velocities in this region.

4.3. Comparisons of Seismic Velocities to Heat Flow

Global seismic tomography reveals positive velocity anomalies beneath all cratons and characterizes the seismic lithosphere as a high-velocity lid overlying the low-velocity asthenosphere (Artemieva, 2009; Polet & Anderson, 1995). Arguments have concentrated on the compositional versus noncompositional (thermal) contributions to the variation of continental seismic velocities (Artemieva, 2009; Deschamps et al., 2002; Forte & Perry, 2000). The diverse mantle regimes sampled by our model, which range from the Precambrian basement of the WCSB to a Phanerozoic Cordilleran orogen, offers a rare opportunity to examine age-dependent variations in these physical properties and their effects on the seismic velocities of the continental lithosphere.

Seismic velocity and heat flow have been widely used to infer the temperature and thermal thickness of mantle lithosphere, which is typically defined by the depth of 1,300 °C adiabat (Artemieva, 2006; Goes et al., 2000; Röhm et al., 2000). The correlations among thermal thickness, seismic velocity, and tectonic age have been examined on both global (Artemieva, 2006, 2009; Artemieva & Mooney, 2001; Röhm et al., 2000) and continental (Furlong et al., 1995; Godey et al., 2004; Goes et al., 2000) scales. In this study, we investigate this correlation beneath the western margin of Laurentia based on the combination of our models and a compilation of thermal data from Majorowicz (2018). The heat flow varies substantially from high values (80 ± 10 mW/m^2) in the northern part of our study region to low values (50 ± 7 mW/m^2) in southern

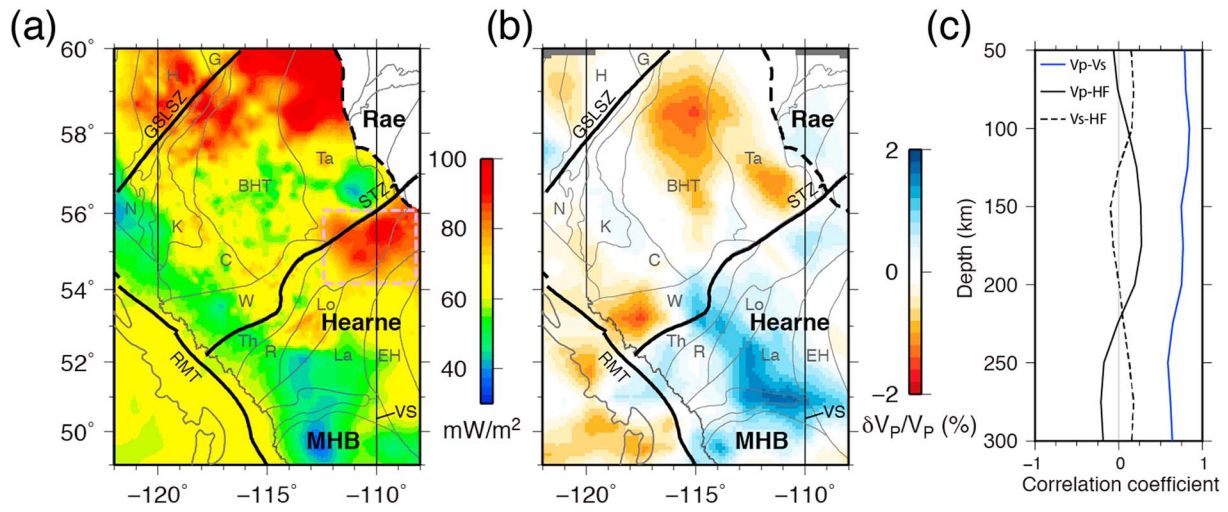

Figure 12. (a) Heat flow of the WCSB (Majorowicz, 2018). The enclosed area shows high heat flow, which overlaps with an earlier reported crustal low-velocity zone (Chen et al., 2015). (b) Averaged *P* wave velocity perturbations between 50 and 300-km depths. (c) Correlation between heat flow and seismic velocity at each depth. The blue line indicates the correlation between *P* and *S* velocities.

Alberta (Figure 12a). The latter region covers the Archean-aged Hearne and MHB cratons that are underlain by the highest- (>2%) velocity perturbations (Figure 12b) and generally agrees with the average Archean heat flow (42 ± 10 mW/m^2) in the Canadian Shield (Jaupart et al., 1998). However, the overall regional correlation between the seismic velocities and the surface heat flow is low, showing coefficients (typically less than 0.2, Figure 12c) that are statistically insignificant. Our measurement is similar to the low correlations found in the upper mantle of Europe (Goes et al., 2000) but deviates from a moderate anticorrelation (coefficient of 0.6) trend reported in the earlier continental-scale studies of North America (Godey et al., 2004; Röhm et al., 2000). This strong regional variability could reflect a change in the dominant heat flow sources of the crustal heat production and mantle heat flow. Earlier studies have suggested that the thickness of high heat production layer was required to vary by as much as a factor of 2 to account for the large heat flow perturbation across the WCSB (see Figure 12a; Majorowicz, 2018). This argument is supported by a pronounced heat flow high that flanks the STZ to the south in central Alberta (see Figure 12a), a region intruded by granitic rocks at upper-middle crustal depths (Bouzidi et al., 2002; Chen et al., 2015). The thick (>10-km) granitic layer that enriched in heat generation elements could serve as a sufficient heat reservoir and cause an elevated heat flow in this region. The dominant crustal contribution of the surface heat flow infers a relatively constant and low mantle heat flux (15 ± 5 mW/m^2; Majorowicz, 2018) beneath the WCSB, which is supported by the lack of correlation between mantle velocity and heat flow in our study.

4.4. Comparisons of Seismic Velocities to Gravity

Globally, a pronounced correlation between the crustal age and mantle chemical composition has been suggested to reflect the secular depletion of the mantle lithosphere (Griffin et al., 2008; Jordan, 1988). The degree of depletion generally increases with tectonic age (Artemieva, 2009; Lee et al., 2011). For instance, the Archean mantle is characterized by a strongly depleted composition due to loss of Fe and Al during secular melt extraction, whereas Proterozoic and Phanerozoic lithospheres show intermediate and fertile compositions, respectively (Artemieva, 2009; Griffin et al., 2003). A key factor that determines the degree of depletion is the iron content in the mantle olivine (Deschamps et al., 2002), which is quantitatively defined as Mg number (Mg# = Mg/[Mg + Fe]). There is a general decreasing trend of density with increasing Mg# (Lee, 2003; Schutt & Lesher, 2006). Although direct measurement of Mg# (i.e., the degree of depletion) is hampered by a lack of xenolith samples in the WCSB, density variations reflected from the gravity field provide the first-order constraints on lithospheric compositions.

Earlier studies have focused either on a direct examination (e.g., Bouzidi et al., 2002; Ross et al., 1991; Pilkingtonet al., 2000) or modeling (e.g., Eaton & Hope, 2003; Hope & Eaton, 2002; Lemieux et al., 2000; Lynn et al., 2005) of gravity data to resolve the subsurface structures of the WCSB. Our study benefits from

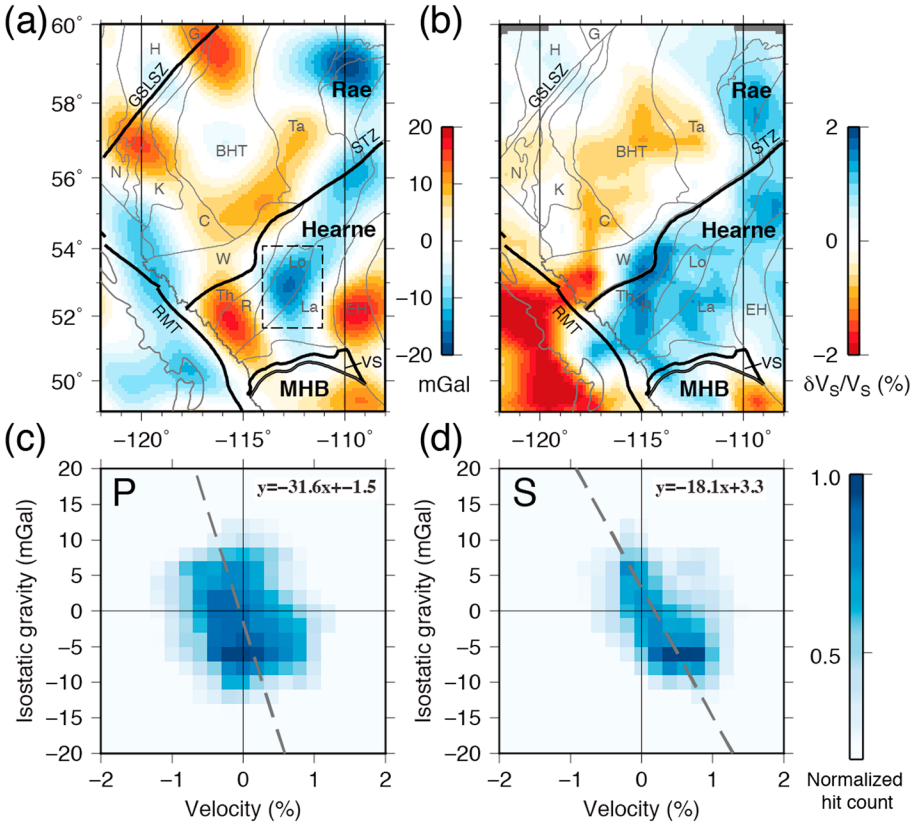

Figure 13. (a) Long-wavelength isostatic gravity field (Jobin et al., 2017). The enclosed region highlights a significant gravity low in the southern Hearne province. The thick lines indicate the major tectonic boundaries. (b) Averaged shear velocities between 100 and 300-km depths. The gravity lows are generally underlain by high shear velocities to the south of the Snowbird Tectonic Zone. Correlation between isostatic gravity and (c) *P* and (d) *S* velocities. The color shows the normalized hit counts of grid points with specific gravity and velocity values. The dashed line indicates a weighted linear regression computed using grids with number of hits larger than 0.6 to capture the regional trend. For example, the Cordilleran region is excluded due to low hit count.

the new mantle velocity constraints and allows a detailed examination of subcrustal structures and the associated density variations. We use isostatic-corrected Bouguer anomaly (i.e., isostatic anomaly) to minimize the effects of deep crustal roots (e.g., ~50 km near the foreland thrust-and-fold belt; Gu et al., 2018) on the measured gravity fields. The resulting (isostatic) anomaly represents an integrated effect of the mass distribution in the lithosphere, contributed by diverse sources with different characteristic wavelengths. To isolate various source contributions, we filter the gravity data into intermediate wavelength (280–1,400 km) to suppress the shallow structures assuming that the maximum source depth is a quarter of the wavelength. As a result, the selected corner frequency (280 km) effectively removes gravity anomalies from sources shallower than 70 km, a depth range poorly constrained by our tomographic model.

A significant isostatic low is observed in the southern Hearne province (Figure 13a), which suggests that the topography is isostatically overcompensated (i.e., the estimated root is smaller than actual; Lowrie, 2007). However, this argument is inconsistent with a relatively shallow Moho in this region (Bouzidi et al., 2002; Gu et al., 2018) and implies a possible deeper (subcrustal) gravity source. Considering a dominant upper mantle contribution to the gravity anomaly beneath the North American craton (Thompson et al., 2011), we suggest that this isostatic low is likely caused by the deep cratonic root of the southern Hearne province (Figure 13b). On the other hand, northern Alberta shows a broad region of isostatic high in association with a shallow lithosphere (see Figure 11c). A quantitative comparison shows a clear negative correlation between the filtered isostatic gravity and velocities (Figures 13c and 13d), suggesting a possible common controlling factor for both physical properties. In other words, it is conceivable that the highly depleted cratons (e.g.,

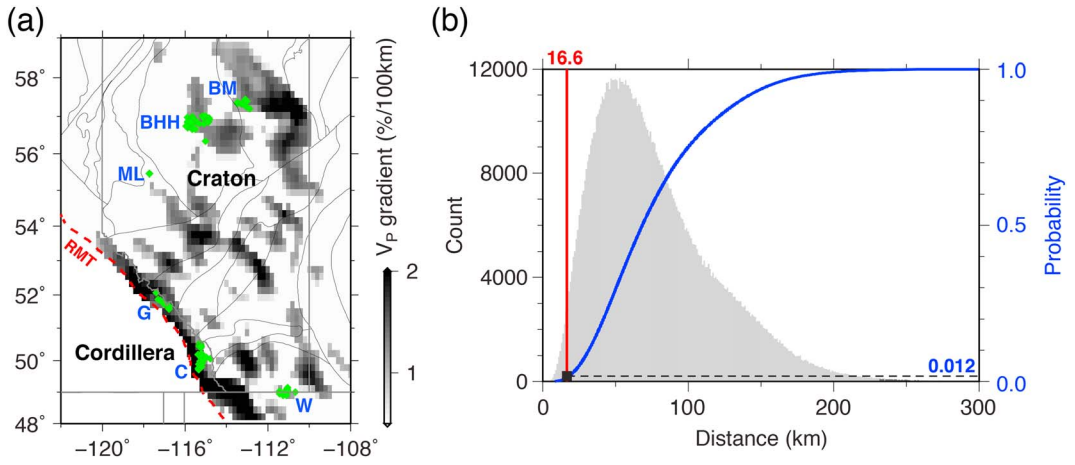

Figure 14. (a) Average *P* velocity gradient of craton within the diamond stability field (150–250-km depths). The green diamonds mark the location of kimberlite and lamproite intrusions from World Kimberlite database (Faure, 2010). Abbreviation: BH, Birch Mountains; BHH, Buffalo Head Hills; C, Cross; G, Golden; ML, Mountain Lake; W, Williams. (b) Monte Carlo simulation of kimberlite locations. The observed average distance between kimberlite clusters and the high-velocity gradient zones (HVGZ) is indicated by the red line. The blue line shows the cumulative probability of the average kimberlite-HVGZ distance distribution (histogram). The black square indicates the intersection of these two lines. The horizontal dashed line marks the probability that kimberlite clusters distribute at distances less than the observed value (16.6 km).

Hearne province) in our region, which are characterized by high seismic velocities and low densities, are the products of extensive melt extraction of the Archean mantle lithospheres (Lee, 2003; Schutt & Lesher, 2006). This interpretation is consistent with global trends of major iron-depleted deep lithospheric keels in the Slave/Hearne cratons of the Canadian Shield, the western part of the East European craton, the Siberian craton, and south and west African cratons (Artemieva, 2009).

4.5. Correlation With Kimberlite Locations

The cratonic basement of the WCSB has been intruded by several kimberlite groups during the Mesozoic. Our new seismic model permits a detailed examination of the potential relationship between the deep lithospheric structure and shallow kimberlite deposits. To this end, we calculate the average horizontal *P* velocity gradient between 150 and 250-km depths, a range with ideal pressure-temperature conditions for diamond preservation, and the resulting model shows an excellent spatial correlation between the HVGZ and kimberlite sites (Figure 14a). The mean distance between kimberlite clusters and the nearest HVGZ is calculated by a weighted average based on the number of reported samples (Faure, 2010). Our result shows that the kimberlites are generally distributed within 20-km lateral distance from the HVGZ. To examine the statistical significance of our observations, we perform a Monte Carlo simulation while assuming that the kimberlite locations follow a uniform distribution; that is, the kimberlite has equal probability to fall into any grid in the map area. A total of 10^6 simulations are conducted, and an average kimberlite-HVGZ distance of all six clusters is calculated in each realization. The summarized distribution resembles a skewed Gaussian function with a gradually tapering tail at greater distances (Figure 14b). Our observed value intersects with the cumulative density function at 1.2%, a low probability to recover the observed kimberlite distribution pattern, which suggests that the observed spatial association is unlikely to be coincidental.

These results establish a statistically robust relationship between the kimberlites and mantle lithospheric structures in the WCSB. Similar kimberlite distribution patterns were reported in Australia, where surface wave tomography shows that the diamondiferous intrusion appears preferentially at the craton margins (Jaques & Milligan, 2004), and the nearby THO, in which the Cretaceous diamondiferous kimberlites occur above or near the rims of a pronounced low-velocity anomaly. These observations could reflect the regional/local structural controls on the diamond concentration, which is also evidenced by the alignment of kimberlites with the potential field discontinuities (Jaques & Milligan, 2004). Furthermore, the convincing link between the kimberlite and HVGZ could suggest either preferential formation or intrusion of the kimberlites. On a global scale, the analyses of kimberlite distributions have revealed a strong spatial association with the mantle hot spots (Crough et al., 1980) and plume-generation zones (Torsvik et al., 2010). On the other

hand, regional surveys of the eastern North American craton and the THO respectively attributed the kimberlite and the associated low-velocity anomalies to hot spot track (Boyce et al., 2016) and plume erosion of the mantle lithosphere (Bank et al., 1998). The close spatial affinity between the THO and our study region (a few hundreds of kilometers apart) favors the same mechanism involving mantle plume activities (Davies et al., 2004), though further studies will be required to establish a more convincing relationship between these two regions. Alternatively, the HVGZ could have delineated a preexisting weak or boundary zone in the lithosphere, which provides a practical pathway for the eruption of the kimberlite magma. The metasomatic enrichment during the eruption process could have reworked the lithosphere, which results in significantly reduced lithosphere velocities in an otherwise intact cratonic mantle and produces a large velocity gradient near the eruption site.

5. Conclusions

This study provides an updated appraisal of the lithospheric structures beneath the WCSB, and the key conclusions are as follows:

1. The cratonic lithospheres, characterized by high velocities beneath the BHT, Wabamun domain, Hearne province, and MHB, are well correlated with their overlying crustal domains. Lithosphere thickness varies from ~300 km beneath the Archean Hearne craton to an average of ~160 km underlying the Proterozoic terranes in northern Alberta.
2. Pronounced low-velocity zones are found beneath the Canadian Cordillera, which contrasts sharply with the high velocities beneath the bounding craton(s). Their transition defines a sharp seismic Cordillera-Craton boundary that marks a potential collisional suture of the orogenic belts.
3. Mantle seismic velocity shows no apparent correlation with surface heat flow, which suggests a dominant crustal contribution to the regional variability. On the other hand, a clear relationship (i.e., anticorrelation) exists between velocity and long-wavelength isostatic gravity, suggesting melt depletion and enrichment beneath the cratonic mantle lithosphere of western Laurentia.
4. The kimberlite xenoliths occur near the zones of high-velocity gradient. Monte Carlo simulation shows that this spatial correlation is statistically robust with a probability of less than 2% to occur by chance. The concentration pattern could reflect either preferential formation or eruption of kimberlites at the lithospheric weak zones marked by the high-velocity gradients.

Finally, we are able to provide new *P* and *S* velocity models of mantle lithosphere based on the most updated broadband data set available in the WCSB. Compared to past regional- and continental-scale models, our high-resolution tomography offers improved seismic constraints on the morphology and composition of the cratonic lithosphere. Through an integration of mantle velocity with surface heat flow, isostatic gravity anomaly, and kimberlite spatial distribution, our study sheds new light on the formation and postassembly modifications of western Laurentia.

Acknowledgments
We thank Jacek Majorowicz for kind support for our heat flow analysis. We thank the Global Seismology Group at the University of Alberta for the field supports. Seismic data for USArray, RAVEN, and CANOE networks are provided by IRIS Data Management Center (http://ds.iris.edu/ds/nodes/dmc/). Seismic data for CNSN network could be requested from Canadian National Data Center (http://www.earthquakescanada.nrcan.gc.ca/stndon/CNDC/index-en.php). Traveltime data could be accessed through website https://sites.google.com/a/ualberta.ca/seisworld/data. This work was supported by the National Sciences and Engineering Research Council of Canada (NSERC; RGPIN-2017-06093). We thank two anonymous reviewers and the Associate Editor for constructive comments that have significantly improved this paper.

References

Artemieva, I. M. (2006). Global 1 × 1 thermal model TC1 for the continental lithosphere: Implications for lithosphere secular evolution. *Tectonophysics*, *416*(1), 245–277.
Artemieva, I. M. (2009). The continental lithosphere: Reconciling thermal, seismic, and petrologic data. *Lithos*, *109*(1), 23–46.
Artemieva, I. M., & Mooney, W. D. (2001). Thermal thickness and evolution of Precambrian lithosphere: A global study. *Journal of Geophysical Research*, *106*(B8), 16,387–16,414.
Aulbach, S., Griffin, W. L., O'Reilly, S. Y., & McCandless, T. E. (2004). Genesis and evolution of the lithospheric mantle beneath the Buffalo Head Terrane, Alberta (Canada). *Lithos*, *77*(1–4), 413–451. https://doi.org/10.1016/j.lithos.2004.04.020
Banas, A., Stachel, T., Muehlenbachs, K., & McCandless, T. E. (2007). Diamonds from the Buffalo Head Hills, Alberta: Formation in a non-conventional setting. *Lithos*, *93*(1–2), 199–213.
Bank, C., Bostock, M. G., Ellis, R. M., Hajnal, Z., & VanDecar, J. C. (1998). Lithospheric mantle structure beneath the Trans-Hudson Orogen and the origin of diamondiferous kimberlites. *Journal of Geophysical Research*, *103*(B5), 10,103–10,114. https://doi.org/10.1029/97JB03746
Bao, X., & Eaton, D. W. (2015). Large variations in lithospheric thickness of western Laurentia: Tectonic inheritance or collisional reworking? *Precambrian Research*, *266*, 579–586. https://doi.org/10.1016/j.precamres.2015.05.010
Bao, X., Eaton, D. W., & Gu, Y. J. (2016). Rayleigh wave azimuthally anisotropic phase velocity maps beneath western Canada. *Journal of Geophysical Research: Solid Earth*, *121*, 1821–1834. https://doi.org/10.1002/2015JB012453
Bao, X., Eaton, D. W., & Guest, B. (2014). Plateau uplift in western Canada caused by lithospheric delamination along a craton edge. *Nature Geoscience*, *7*(11), 830–833. https://doi.org/10.1038/ngeo2270
Beaumont, C. (1981). Foreland basins. *Group*, (il), 1–11. https://doi.org/10.1002/9781444303810
Bedle, H., & van der Lee, S. (2009). S velocity variations beneath North America. *Journal of Geophysical Research*, *114*, B07308. https://doi.org/10.1029/2008JB005949

Boerner, D. E., Kurtz, R. D., Craven, J. A., Rondenay, S., & Qian, W. (1995). Buried Proterozoic foredeep under the Western Canada Sedimentary Basin? *Geology*, *23*(4), 297–300. https://doi.org/10.1130/0091-7613(1995)023<0297:BPFUTW>2.3.CO;2

Boerner, D. E., Kurtz, R. D., Craven, J. A., Ross, G. M., & Jones, F. W. (2000). A synthesis of electromagnetic studies in the Lithoprobe Alberta Basement Transect: Constraints on Paleoproterozoic indentation tectonics. *Canadian Journal of Earth Sciences*, *37*(11), 1509–1534. https://doi.org/10.1139/e00-063

Boerner, D. E., Kurtz, R. D., Craven, J. A., Ross, G. M., Jones, F. W., & Davis, W. J. (1999). Electrical conductivity in the Precambrian lithosphere of western Canada. *Science*, *283*(5402), 668–670. https://doi.org/10.1126/science.283.5402.668

Bond, G. C., & Kominz, M. A. (1984). Construction of tectonic subsidence curves for the early Paleozoic miogeocline, southern Canadian Rocky Mountains: Implications for subsidence mechanisms, age of breakup, and crustal thinning. *Geological Society of America Bulletin*, *95*(2), 155–173. https://doi.org/10.1130/0016-7606(1984)95<155:COTSCF>2.0.CO;2

Bouzidi, Y., Schmitt, D. R., Burwash, R. A., & Kanasewich, E. R. (2002). Depth migration of deep seismic reflection profiles: Crustal thickness variations in Alberta. *Canadian Journal of Earth Sciences*, *39*(3), 331–350. https://doi.org/10.1139/e01-080

Boyce, A., Bastow, I. D., Darbyshire, F. A., Ellwood, A. G., Gilligan, A., Levin, V., & Menke, W. (2016). Subduction beneath Laurentia modified the eastern North American cratonic edge: Evidence from P wave and S wave tomography. *Journal of Geophysical Research: Solid Earth*, *121*, 5013–5030. https://doi.org/10.1002/2016JB012838

Canil, D., Schulze, D. J., Hall, D., Hearn Jr, B. C., & Milliken, S. M. (2003). Lithospheric roots beneath western Laurentia: The geochemical signal in mantle garnets. *Canadian Journal of Earth Sciences*, *40*(8), 1027–1051. https://doi.org/10.1139/e03-003

Cant, D. J., & Stockmal, G. S. (1989). The Alberta foreland basin: Relationship between stratigraphy and Cordilleran terrane-accretion events. *Canadian Journal of Earth Sciences*, *26*(10), 1964–1975. https://doi.org/10.1139/e89-166

Carlson, S. M., Hillier, W. D., & Hood, C. T. (1999). The Buffalo Hills kimberlites: A newly-discovered diamondiferous kimberlite province in north-central Alberta, Canada. in 8th International Kimberlite Conference, pp. 109–116.

Chacko, T., de, S. K., Creaser, R. A., & Muehlenbachs, K. (2000). Tectonic setting of the Taltson magmatic zone at 1.9-2.0 Ga: A granitoid-based perspective. *Canadian Journal of Earth Sciences*, *37*(11), 1597–1609. https://doi.org/10.1139/e00-029

Chen, Y., Gu, Y. J., Dokht, R. M. H., & Sacchi, M. D. (2015). Crustal imprints of Precambrian orogenesis in western Laurentia. *Journal of Geophysical Research: Solid Earth*, *120*, 6993–7012. https://doi.org/10.1002/2014JB011353

Chen, Y., Gu, Y. J., & Hung, S.-H. (2017). Finite-frequency P-wave tomography of the Western Canada Sedimentary Basin: Implications for the lithospheric evolution in Western Laurentia. *Tectonophysics*, *698*, 79–90. https://doi.org/10.1016/j.tecto.2017.01.006

Clowes, R. M. (2010). Initiation, development, and benefits of Lithoprobe—Shaping the direction of Earth science research in Canada and beyond this article is one of a series of papers published in this special issue on the theme *Lithoprobe*: Parameters, processes, and the. *Canadian Journal of Earth Sciences*, *47*(4), 291–314. https://doi.org/10.1139/E09-074

Clowes, R. M., Zelt, C. A., Amor, J. R., & Ellis, R. M. (1995). Lithospheric structure in the southern Canadian Cordillera from a network of seismic refraction lines. *Canadian Journal of Earth Sciences*, *32*(10), 1485–1513. https://doi.org/10.1139/e95-122

Coney, P. J. (1989). Structural aspects of suspect terranes and accretionary tectonics in western North America. *Journal of Structural Geology*, *11*(1–2), 107–125.

Courtier, A. M., Gaherty, J. B., Revenaugh, J., Bostock, M. G., & Garnero, E. J. (2010). Seismic anisotropy associated with continental lithosphere accretion beneath the CANOE array, northwestern Canada. *Geology*, *38*(10), 887–890. https://doi.org/10.1130/G31120.1

Crough, S. T., Morgan, W. J., & Hargraves, R. B. (1980). Kimberlites: Their relation to mantle hotspots. *Earth and Planetary Science Letters*, *50*(1), 260–274.

Dahlen, F. A., Hung, S.-H., & Nolet, G. (2000). Fréchet kernels for finite-frequency traveltimes—I. Theory. *Geophysical Journal International*, *141*(1), 157–174. https://doi.org/10.1046/j.1365-246X.2000.00070.x

Dalton, C. A., Gaherty, J. B., & Courtier, A. M. (2011). Crustal V_S structure in northwestern Canada: Imaging the Cordillera-craton transition with ambient noise tomography. *Journal of Geophysical Research*, *116*, B12315. https://doi.org/10.1029/2011JB008499

Darbyshire, F. A., Eaton, D. W., & Bastow, I. D. (2013). Seismic imaging of the lithosphere beneath Hudson Bay: Episodic growth of the Laurentian mantle keel. *Earth and Planetary Science Letters*, *373*, 179–193.

Davies, R. M., Griffin, W. L., O'Reilly, S. Y., & McCandless, T. E. (2004). Inclusions in diamonds from the K14 and K10 kimberlites, Buffalo Hills, Alberta, Canada: Diamond growth in a plume? *Lithos*, *77*(1–4), 99–111. https://doi.org/10.1016/j.lithos.2004.04.008

De, S. K., Chacko, T., Creaser, R. A., & Muehlenbachs, K. (2000). Geochemical and Nd-Pb-O isotope systematics of granites from the Taltson Magmatic Zone, NE Alberta: Implications for early Proterozoic tectonics in western Laurentia. *Precambrian Research*, *102*(3–4), 221–249. https://doi.org/10.1016/S0301-9268(00)00068-1

Deschamps, F., Trampert, J., & Snieder, R. (2002). Anomalies of temperature and iron in the uppermost mantle inferred from gravity data and tomographic models. *Physics of the Earth and Planetary Interiors*, *129*(3), 245–264.

Dickinson, W. R., Kay, S. M., & Ramos, V. A. (2009). Anatomy and global context of the North American Cordillera. In *Backbone of the Americas: Shallow subduction, plateau uplift, and ridge and terrane collision*. *Geological Society of America Memoir, 204*, 1–29.

Eaton, D. W., & Hope, J. (2003). Structure of the crust and upper mantle of the Great Slave Lake shear zone, northwestern Canada, from teleseismic analysis and gravity modelling. *Canadian Journal of Earth Sciences*, *40*(9), 1203–1218. https://doi.org/10.1139/e03-038

Eaton, D. W., Ross, G. M., & Hope, J. (1999). The rise and fall of a cratonic arch: A regional seismic perspective on the Peace River Arch, Alberta. *Bulletin of Canadian Petroleum Geology*, *47*(4), 346–361.

Evenchick, C. (2007). A synthesis of the Jurassic–Cretaceous tectonic evolution of the central and southeastern Canadian Cordillera: Exploring links across the orogen. *Society of America*, *i*(06), 117–145. https://doi.org/10.1130/2007.2433(06).For

Faure, S. (2010). World Kimberlites CONSOREM Database (version 3), Consortium de Recherche en Exploration Minerale CONSOREM, Universite du Quebece Montreal.—2010.—www. consorem. ca.

Fischer, K. M., Ford, H. A., Abt, D. L., & Rychert, C. A. (2010). The lithosphere-asthenosphere boundary. *Annual Review of Earth and Planetary Sciences*, *38*(1), 551–575. https://doi.org/10.1146/annurev-earth-040809-152438

Forte, A. M., & Perry, H. K. C. (2000). Geodynamic evidence for a chemically depleted continental tectosphere. *Science*, *290*(5498), 1940–1944. https://doi.org/10.1126/science.290.5498.1940

Frederiksen, A. W., Bostock, M. G., & Cassidy, J. F. (2001). S-wave velocity structure of the Canadian upper mantle. *Physics of the Earth and Planetary Interiors*, *124*(3), 175–191.

Frederiksen, A. W., Bostock, M. G., Van Decar, J. C., & Cassidy, J. F. (1998). Seismic structure of the upper mantle beneath the northern Canadian Cordillera from teleseismic travel-time inversion. *Tectonophysics*, *294*(1–2), 43–55. https://doi.org/10.1016/S0040-1951(98)00095-X

Furlong, K. P., Spakman, W., & Wortel, R. (1995). Thermal structure of the continental lithosphere: Constraints from seismic tomography. *Tectonophysics*, *244*(1–3), 107–117.

Godey, S., Deschamps, F., Trampert, J., & Snieder, R. (2004). Thermal and compositional anomalies beneath the North American continent. *Journal of Geophysical Research*, *109*, B01308. https://doi.org/10.1029/2002JB002263
Goes, S., Govers, R., & Vacher, P. (2000). Shallow mantle temperatures under Europe from P and S wave tomography. *Journal of Geophysical Research*, *105*(B5), 11,153–11,169.
Griffin, W. L., O'Reilly, S. Y., Abe, N., Aulbach, S., Davies, R. M., Pearson, N. J., et al. (2003). The origin and evolution of Archean lithospheric mantle. *Precambrian Research*, *127*(1-3), 19–41. https://doi.org/10.1016/S0301-9268(03)00180-3
Griffin, W. L., O'Reilly, S. Y., Afonso, J. C., & Begg, G. C. (2008). The composition and evolution of lithospheric mantle: A re-evaluation and its tectonic implications. *Journal of Petrology*, *50*(7), 1185–1204.
Gu, Y. J., & Chen, Y. (2015). From isostasy to Proterozoic underplating: New inferences from crustal thickness and Vp/Vs ratio beneath the Western Canada Sedimentary Basin, in AGU Fall Meeting Abstracts.
Gu, Y. J., Chen, Y., Dokht, R. M. H., & Wang, R. (2018). Precambrian tectonic discontinuities in western Laurentia: Broadband seismological perspectives on the Snowbird and Great Falls tectonic zones. *Tectonics*, *37*, 1411–1434. https://doi.org/10.1029/2017TC004843
Gu, Y. J., Okeler, A., Shen, L., & Contenti, S. (2011). The Canadian Rockies and Alberta Network (CRANE): New constraints on the Rockies and Western Canada Sedimentary Basin. *Seismological Research Letters*, *82*(4), 575–588. https://doi.org/10.1785/gssrl.82.4.575
Gu, Y. J., & Shen, L. (2015). Noise correlation tomography of Southwest Western Canada Sedimentary Basin. *Geophysical Journal International*, *202*(1), 142–162. https://doi.org/10.1093/gji/ggv100
Gu, Y. J., Zhang, Y., Sacchi, M. D., Chen, Y., & Contenti, S. (2015). Sharp mantle transition from cratons to Cordillera in southwestern Canada. *Journal of Geophysical Research: Solid Earth*, *120*, 5051–5069. https://doi.org/10.1002/2014JB011802
Gung, Y., Panning, M., & Romanowicz, B. (2003). Global anisotropy and the thickness of continents. *Nature*, *422*(6933), 707–711.
Heaman, L. M., Kjarsgaard, B. A., & Creaser, R. A. (2004). The temporal evolution of North American kimberlites. *Lithos*, *76*(1–4), 377–397.
Hieronymus, C. F., & Goes, S. (2010). Complex cratonic seismic structure from thermal models of the lithosphere: Effects of variations in deep radiogenic heating. *Geophysical Journal International*, *180*(3), 999–1,012.
Hoffman, P. F. (1988). United plates of America, the birth of a Craton: Early Proterozoic assembly and growth of Laurentia. *Annual Review of Earth and Planetary Sciences*, *16*(1), 543–603. https://doi.org/10.1146/annurev.ea.16.050188.002551
Hoffman, P. F. (1989). Precambrian geology and tectonic history of North America. In *The geology of North America* (Vol. A, pp. 447–512). Boulder: The Geological Soc. Amer. Inc.
Hope, J., & Eaton, D. (2002). Crustal structure beneath the Western Canada Sedimentary Basin: Constraints from gravity and magnetic modelling. *Canadian Journal of Earth Sciences*, *39*(3), 291–312. https://doi.org/10.1139/e01-060
Hung, S. H., Chen, W. P., & Chiao, L. Y. (2011). A data-adaptive, multiscale approach of finite-frequency, traveltime tomography with special reference to P and S wave data from central Tibet. *Journal of Geophysical Research*, *116*, B06307. https://doi.org/10.1029/2010JB008190
Hung, S.-H., Dahlen, F. A., & Nolet, G. (2000). Fréchet kernels for finite-frequency traveltimes: II. Examples. *Geophysical Journal International*, *141*(1), 175–203.
Hung, S. H., Shen, Y., & Chiao, L. Y. (2004). Imaging seismic velocity structure beneath the Iceland hot spot: A finite frequency approach. *Journal of Geophysical Research*, *109*, B08305. https://doi.org/10.1029/2003JB002889
Hyndman, R. D., Currie, C. A., & Mazzotti, S. P. (2005). Subduction zone backarcs, mobile belts, and orogenic heat. *GSA Today*, *15*(2), 4–10. https://doi.org/10.1130/1052-5173(2005)015<4:SZBMBA>2.0.CO;2
Hyndman, R. D., & Lewis, T. J. (1999). Geophysical consequences of the Cordillera-Craton thermal transition in southwestern Canada. *Tectonophysics*, *306*(3–4), 397–422. https://doi.org/10.1016/S0040-1951(99)00068-2
Jaques, A. L., & Milligan, P. R. (2004). Patterns and controls on the distribution of diamondiferous intrusions in Australia. *Lithos*, *77*(1), 783–802.
Jaupart, C., Mareschal, J. C., Guillou-Frottier, L., & Davaille, A. (1998). Heat flow and thickness of the lithosphere in the Canadian Shield. *Journal of Geophysical Research*, *103*(B7), 15,269–15,286. https://doi.org/10.1029/98JB01395
Jobin, D. M., Véronneau, M., & Miles, W. (2017). Isostatic residual gravity anomaly map, Canada/Carte des anomalies isostatiques résiduelles du champ de gravité, Canada. Geological Survey of Canada, Open File 8076.
Johnston, S. T. (2001). The Great Alaskan Terrane Wreck: Reconciliation of paleomagnetic and geological data in the northern Cordillera. *Earth and Planetary Science Letters*, *193*(3), 259–272.
Johnston, S. T. (2008). The Cordilleran Ribbon continent of North America. *Annual Review of Earth and Planetary Sciences*, *36*, 495–530. https://doi.org/10.1146/annurev.earth.36.031207.124331
Jordan, T. H. (1978). Composition and development of the continental tectosphere. *Nature*, *274*(5671), 544–548. https://doi.org/10.1038/274544a0
Jordan, T. H. (1988). Structure and formation of the continental tectosphere. *Journal of Petrology*, *1*, 11–37.
Karato, S., & Wu, P. (1993). Rheology of the upper mantle: A synthesis. *Science*, *260*(5109), 771–778.
Kennett, B. L. N., Engdahl, E. R., & Buland, R. (1995). Constraints on seismic velocities in the Earth from traveltimes. *Geophysical Journal International*, *122*(1), 108–124.
Laske, G., Masters, G., Ma, Z., & Pasyanos, M. (2013). Update on CRUST1. 0—A 1-degree global model of Earth's crust, in Geophys. Res. Abstr, p. 2658.
Lebedev, S., & Nolet, G. (2003). Upper mantle beneath Southeast Asia from S velocity tomography. *Journal of Geophysical Research*, *108*(B1), 2048. https://doi.org/10.1029/2000JB000073
Lee, C. A. (2003). Compositional variation of density and seismic velocities in natural peridotites at STP conditions: Implications for seismic imaging of compositional heterogeneities in the upper mantle. *Journal of Geophysical Research*, *108*(B9), 2441. https://doi.org/10.1029/2003JB002413
Lee, C.-T. A., Luffi, P., & Chin, E. J. (2011). Building and destroying continental mantle. *Annual Review of Earth and Planetary Sciences*, *39*, 59–90.
Lemieux, S., Ross, G. M., & Cook, F. A. (2000). Crustal geometry and tectonic evolution of the Archean crystalline basement beneath the southern Alberta Plains, from new seismic reflection and potential-field studies. *Canadian Journal of Earth Sciences*, *37*(11), 1473–1491. https://doi.org/10.1139/e00-065
Levander, A., Schmandt, B., Miller, M. S., Liu, K., Karlstrom, K. E., Crow, R. S., et al. (2011). Continuing Colorado plateau uplift by delamination-style convective lithospheric downwelling. *Nature*, *472*(7344), 461–465. https://doi.org/10.1038/nature10001
Lowrie, W. (2007). *Fundamentals of geophysics*. New York: Cambridge University Press. https://doi.org/10.1017/CBO9780511807107
Lucas, S. B., Green, A., Hajnal, Z., White, D., Lewry, J., Ashton, K., et al. (1993). Deep seismic profile across. *Nature*, *363*(6427), 339–342. https://doi.org/10.1038/363339a0
Lynn, C. E., Cook, F. A., & Hall, K. W. (2005). Tectonic significance of potential-field anomalies in western Canada: Results from the Lithoprobe SNORCLE transect. *Canadian Journal of Earth Sciences*, *42*(6), 1239–1255. https://doi.org/10.1139/e05-037
Majorowicz, J. A. (2018). Heat flow–heat production relationship not found: What drives heat flow variability of the western Canadian foreland basin? *International Journal of Earth Sciences*, *107*(1), 5–18. https://doi.org/10.1007/s00531-016-1352-x

McDonough, M. R., McNicoll, V. J., Schetselaar, E. M., & Grover, T. W. (2000). Geochronological and kinematic constraints on crustal shortening and escape in a two-sided oblique-slip collisional and magmatic orogen, Paleoproterozoic Taltson magmatic zone, northeastern Alberta. *Canadian Journal of Earth Sciences*, *37*(11), 1549–1573. https://doi.org/10.1139/e00-089

McLellan, M., Schaeffer, A. J., & Audet, P. (2018). Structure and fabric of the crust and uppermost mantle in the Northern Canadian Cordillera from Rayleigh-wave tomography. *Tectonophysics*, *724-725*, 28–41. https://doi.org/10.1016/j.tecto.2018.01.011

McNicoll, V. J., Thériault, R. J., & McDonough, M. R. (2000). Taltson basement gneissic rocks: U-Pb and Nd isotopic constraints on the basement to the Paleoproterozoic Taltson magmatic zone, northeastern Alberta. *Canadian Journal of Earth Sciences*, *37*(11), 1575–1596. https://doi.org/10.1139/e00-034

Mercier, J., et al. (2008). The teleseismic signature of fossil subduction: Northwestern Canada. *Journal of Geophysical Research*, *113*, B04308. https://doi.org/10.1029/2007JB005127

Mercier, J. P., Bostock, M. G., Cassidy, J. F., Dueker, K., Gaherty, J. B., Garnero, E. J., et al. (2009). Body-wave tomography of western Canada. *Tectonophysics*, *475*(3–4), 480–492. https://doi.org/10.1016/j.tecto.2009.05.030

Nieuwenhuis, G., Unsworth, M. J., Pana, D., Craven, J., & Bertrand, E. (2014). Three-dimensional resistivity structure of Southern Alberta, Canada: Implications for Precambrian tectonics. *Geophysical Journal International*, *197*(2), 838–859. https://doi.org/10.1093/gji/ggu068

Pilkington, M., Miles, W. F., Ross, G. M., & Roest, W. R. (2000). Potential-field signatures of buried Precambrian basement in the Western Canada Sedimentary Basin 1. *Canadian Journal of Earth Sciences*, *37*(11), 1453–1471. https://doi.org/10.1139/e00-020

Polet, J., & Anderson, D. L. (1995). Depth extent of cratons as inferred from tomographic studies. *Geology*, *23*(3), 205–208.

Porter, J. W., Price, R. A., & McCrossan, R. G. (1982). The Western Canada Sedimentary Basin. *Philosophical Transactions of the Royal Society of London*, *305*(1489), 169–192. Available at:http://rsta.royalsocietypublishing.org/content/305/1489/169.full.pdf+html

Price, R. A. (1994). Cordilleran tectonics. In G. D. Mossop & I. Shetsen (Eds.), *Geological atlas of the Western Canadian Sedimentary Basin* (pp. 13–24). Calgary: Canadian Society of Petroleum Geologists and Alberta Research Council.

Priestley, K., & Tilmann, F. (2009). Relationship between the upper mantle high velocity seismic lid and the continental lithosphere. *Lithos*, *109*(1), 112–124.

Röhm, A. H. E., Snieder, R., Goes, S., & Trampert, J. (2000). Thermal structure of continental upper mantle inferred from S-wave velocity and surface heat flow. *Earth and Planetary Science Letters*, *181*(3), 395–407. https://doi.org/10.1016/S0012-821X(00)00209-0

Ross, G. M. (2002a). Evolution of Precambrian continental lithosphere in Western Canada: Results from Lithoprobe studies in Alberta and beyond. *Canadian Journal of Earth Sciences*, *39*(3), 413–437. https://doi.org/10.1139/e02-012

Ross, G. M. (2002b). Introduction to special issue of Canadian Journal of Earth Sciences: The Alberta basement transect of Lithoprobe. *Canadian Journal of Earth Sciences*, *39*(3), 287–288. https://doi.org/10.1139/e02-011

Ross, G. M., & Eaton, D. W. (1997). Winagami reflection sequence: Seismic evidence for postcollisional magmatism in the Proterozoic of western Canada. *Geology*, *25*(3), 199–202. https://doi.org/10.1130/0091-7613(1997)025<0199:WRSSEF>2.3.CO;2

Ross, G. M., & Eaton, D. W. (2002). Proterozoic tectonic accretion and growth of western Laurentia: Results from Lithoprobe studies in northern Alberta. *Canadian Journal of Earth Sciences*, *39*(3), 313–329. https://doi.org/10.1139/e01-081

Ross, G. M., Eaton, D. W., Boerner, D. E., & Miles, W. (2000). Tectonic entrapment and its role in the evolution of continental lithosphere: An example from the Precambrian of western Canada. *Tectonics*, *19*(1), 116–134. https://doi.org/10.1029/1999TC900047

Ross, G. M., Milkereit, B., Eaton, D., White, D., Kanasewich, E. R., & Burianyk, M. J. A. (1995). Paleoproterozoic collisional orogen beneath the Western Canada Sedimentary Basin imaged by Lithoprobe crustal seismic-reflection data. *Geology*, *23*(3), 195–199. https://doi.org/10.1130/0091-7613(1995)023<0195:PCOBTW>2.3.CO;2

Ross, G. M., Parrish, R. R., Villeneuve, M. E., & Bowring, S. A. (1991). Geophysics and geochronology of the crystalline basement of the Alberta Basin, western Canada. *Canadian Journal of Earth Sciences*, *28*(4), 512–522. https://doi.org/10.1139/e91-045

Schaeffer, A. J., & Lebedev, S. (2014). Imaging the North American continent using waveform inversion of global and USArray data. *Earth and Planetary Science Letters*, *402*, 26–41.

Schultz, R., & Stern, V. (2015). The Regional Alberta Observatory for Earthquake Studies Network (RAVEN). *CSEG Recorder*, *40*(8), 34–37.

Schutt, D. L., & Lesher, C. E. (2006). Effects of melt depletion on the density and seismic velocity of garnet and spinel lherzolite. *Journal of Geophysical Research*, *111*, B05401. https://doi.org/10.1029/2003JB002950

Shragge, J., Bostock, M. G., Bank, C. G., & Ellis, R. M. (2002). Integrated teleseismic studies of the southern Alberta upper mantle. *Canadian Journal of Earth Sciences*, *39*(3), 399–411. https://doi.org/10.1139/e01-084

Sigloch, K., McQuarrie, N., & Nolet, G. (2008). Two-stage subduction history under North America inferred from multiple-frequency tomography. *Nature Geoscience*, *1*(7), 458–462. https://doi.org/10.1038/ngeo231

Sleep, N. H. (2005). Evolution of the continental lithosphere. *Annual Review of Earth and Planetary Sciences*, *33*, 369–393.

Stewart, J. H. (1972). Initial deposits in the Cordilleran geosyncline: Evidence of a late Precambrian (< 850 my) continental separation. *Geological Society of America Bulletin*, *83*(5), 1345–1360. https://doi.org/10.1130/0016-7606(1972)83[1345:IDITCG]2.0.CO;2

Thompson, D. A., Helffrich, G., Bastow, I. D., Kendall, J. M., Wookey, J., Eaton, D. W., & Snyder, D. B. (2011). Implications of a simple mantle transition zone beneath cratonic North America. *Earth and Planetary Science Letters*, *312*(1-2), 28–36. https://doi.org/10.1016/j.epsl.2011.09.037

Torsvik, T. H., Burke, K., Steinberger, B., Webb, S. J., & Ashwal, L. D. (2010). Diamonds sampled by plumes from the core-mantle boundary. *Nature*, *466*(7304), 352–355. https://doi.org/10.1038/nature09216

VanDecar, J. C., & Crosson, R. S. (1990). Determination of teleseismic relative phase arrival times using multi-channel cross-correlation and least squares. *Bulletin of the Seismological Society of America*, *80*(1), 150–169.

Villeneuve, M. E., Ross, G. M., Theriault, R. J., & Miles, W. (1993). Tectonic subdivision and U-Pb geochronology of the crystalline basement of the Alberta Basin, western Canada. *Bulletin Geological Survey of Canada*, *447*.

Welford, J. K., & Clowes, R. M. (2006). Three-dimensional seismic reflection investigation of the upper crustal Winagami sill complex of northwestern Alberta, Canada. *Geophysical Journal International*, *166*(1), 155–169. https://doi.org/10.1111/j.1365-246X.2006.02805.x

Wright, G. N., McMechan, M. E., & Potter, D. E. G. (1994). Structure and architecture of the Western Canada sedimentary basin. In *Geological atlas of the Western Canada sedimentary basin* (pp. 25–40). Edmonton, Alberta: Alberta Research Council. Available at:http://www.ags.gov.ab.ca/publications/wcsb_atlas/a_ch03/ch_03.html

Yuan, H., French, S., Cupillard, P., & Romanowicz, B. (2014). Lithospheric expression of geological units in central and eastern North America from full waveform tomography. *Earth and Planetary Science Letters*, *402*, 176–186. https://doi.org/10.1016/j.epsl.2013.11.057

Yuan, H., & Romanowicz, B. (2010). Lithospheric layering in the North American craton. *Nature*, *466*(7310), 1063–1068. https://doi.org/10.1038/nature09332

Zaporozan, T., Frederiksen, A. W., Bryksin, A., & Darbyshire, F. (2018). Surface-wave images of western Canada: Lithospheric variations across the Cordillera–Craton boundary. *Canadian Journal of Earth Sciences*, *999*, 1–10.